

Experimental Study of the PVTX Properties of the System H₂O-CH₄

Fang Lin

Dissertation submitted to the faculty of the Virginia Polytechnic Institute and State University in partial fulfillment of the requirements for the degree of

Doctor of Philosophy in Geosciences

Committee

Robert J. Bodnar, chair

Patricia Dove

J. Fred Read

Madeline Schreiber

Amadeu Sum

September 23, 2005
Blacksburg, VA

Keywords: (H₂O-CH₄ system, synthetic fluid inclusions, PVTX properties, Raman spectroscopy, phase equilibria, methane hydrate)

Copyright © 2005, Fang Lin

Experimental Study of the PVTX Properties of the System H₂O-CH₄

Fang Lin

ABSTRACT

The system H₂O-CH₄ is found in a variety of geological environments in the earth's crust, from sedimentary basins to low grade metamorphic terrains. Knowledge of the Pressure-Volume-Temperature-Composition (PVTX) properties of the H₂O-CH₄ system is necessary to understand the role that these fluids play in different geological environments. In this study the properties of the H₂O-CH₄ fluid system at elevated temperatures and pressures has been investigated experimentally to determine the PVTX properties of H₂O-CH₄ fluids in the P-T range equivalent to late diagenetic to low grade metamorphic environments, and X_{CH₄} ≤ 4 mol%. A study has also been conducted to determine methane hydrate stability over the temperature range of -40~20°C. Synthetic fluid inclusions were employed in both studies as miniature autoclaves.

Experimental data for the PVTX properties of H₂O-CH₄ fluids under late diagenetic to low grade metamorphic conditions was used to calculate the slopes of iso-T_h lines (the line connecting the P-T conditions of the inclusions at formation and at homogenization) at different PTX conditions. An empirical equation to describe the slope of iso-T_h line as a function of homogenization temperature and fluid composition was developed. The equation is applicable to natural H₂O-CH₄ fluid inclusions up to 500°C and 3 kilobars, for fluid compositions ≤ 4 mol% CH₄.

The Raman peak position of CH₄ gas is a function of the pressure and temperature. This relationship was used to determine the pressure along the methane hydrate stability curve in the H₂O-CH₄ system. The combined synthetic fluid inclusion, microthermometry and Raman spectroscopy method is a novel experimental approach to determine the P-T stability conditions of methane hydrates. The method is fast compared to conventional methods, and has the potential to be applied to study other gas hydrate systems.

Acknowledgements

My advisor, Dr. Robert J. Bodnar, provided extensive and excellent help for me during the past several years. I am extremely grateful to him for a number of things. I thank him for bringing me to the Department of Geosciences at Virginia Tech, which turned out to be a great place to do science. I thank him for his outstanding teaching on ways of thinking and approaches to scientific problems, and for the opportunities that he generously extended to practice and learn. I also thank him for suggesting the projects, providing guidance and full support during the past five years. Without him, I would not be able to accomplish what I have accomplished.

I would also like to acknowledge my committee: Dr. Patricia Dove, Dr. J. Fred Read, Dr. Madeline Schreiber and Dr. Sum, for their encouraging, enlightenment and constructive advice.

The staff members in the Department of Geosciences are thanked for their excellent service. They made this department an extremely pleasant place to study. My special thanks go to Mr. Charles Farley for his excellent technical assistance and willingness to help at all the time. Ms. Connie Lowe is also specially thanked for her outstanding administrative service, her warm-heart and passion for student affairs is a great resource to resolve the issues outside of research.

The graduate students in this department, past and present, have helped to create a very joyful environment to study too. I especially thank them for their appreciation of diversity and their kindness to help students from different cultural background.

My husband, Zhiyong, deserves many pages of thanks for all he's done over the several years to encourage and support me. I feel very blessed to find this man in my life, who truly loves me and support me in every way he can. His warm words during the down time and his generous offer on insights of research problems from an outsider's view were very helpful.

Finally, I would like to acknowledge my family in China. Thanks to my father, although he passed away fifteen years ago, the value that he placed on education, persistence and responsibility in my childhood helped me out of many difficult situations. My mother is thanked for her selfish-less great love for me. She demonstrated in many ways that she could sacrifice anything for my bright future. I thank my sister for taking care of our mother while I am away from home. I also thank my parents-in-law, for their understanding and love, thank my teachers and friends in China, for encouraging me to explore the world and being supportive.

Table of Contents

Abstract	ii
Acknowledgements	iii
Table of Contents	iv
List of Tables	vi
List of Figures	vii
Chapter 1 – Introduction	1
Chapter 2 – Experimental determination of the PVTX properties of H₂O-CH₄ to 500°C, 3 kbars and X_{CH₄}≤4mol%	3
<i>Abstract</i>	3
<i>Introduction</i>	4
<i>Experimental Methods</i>	5
Starting Materials and Sample Preparation	5
Effect of Formation Conditions on Fluid Composition	10
Microthermometric Analysis	12
<i>Results and Discussion</i>	12
<i>Summary</i>	16
<i>References</i>	18
<i>Tables</i>	20
<i>Figures</i>	27
Chapter 3 – Determination of the P-T stability limits for methane hydrate using a combined synthetic fluid inclusion and Raman spectroscopic technique	36
<i>Abstract</i>	36

<i>Introduction</i>	37
<i>Experimental and Analytical Methods</i>	39
Formation of synthetic fluid inclusions	40
Microthermometric analysis of synthetic fluid inclusions	41
Raman Analysis	44
<i>Results and Discussion</i>	48
Effect of temperature and pressure on the CH ₄ peak position	48
Determination of methane hydrate stability limits	50
Hydrate stability limits from analyses of single inclusions	51
<i>Error Analysis</i>	54
<i>Summary</i>	56
<i>References</i>	58
<i>Tables</i>	62
<i>Figures</i>	64
Chapter 4 – Methane Raman n1 band position correlates with fluid density and interactions at the molecular level	73
<i>References</i>	83
<i>Tables</i>	85
<i>Figures</i>	86

List of Tables

Chapter 2

Table 1 Formation condition and homogenization temperatures measured for the synthetic inclusions	22
Table 2 Slope of iso- T_h lines calculated for each experimental composition	24
Table 3 Fitting parameters for equation (4)	26

Chapter 3

Table 1 Formation conditions of the synthetic fluid inclusions	62
Table 2 Fitting parameters in equation (2)	63

Chapter 4

Table 1 Formation conditions of the synthetic fluid inclusions	85
---	-----------

List of Figures

Chapter 2

- Figure 1** Comparison of the predicted versus measured CH₄ concentration of the synthetic fluid inclusions 27
- Figure 2** Comparison of the predicted versus measured CH₄ concentration produced using older (a-d) and fresh (e-h) Al₃C₄ to generate CH₄ 28
- Figure 3** X-ray powder diffraction pattern of the solid material remaining in the capsule at the end of an experiment 29
- Figure 4** Comparison of the effect of assumed reaction stoichiometry on the predicted composition of H₂O-CH₄ fluids generated by the Al₃C₄ - H₂O reaction 30
- Figure 5** Raman spectra of the synthetic fluid inclusions trapped at various temperatures from 300° to 700°C 31
- Figure 6** Relationship between homogenization temperature (T_h) and CH₄ concentration for inclusions trapped at 300°C, 400°C and 500°C and pressures of 1-3 kbars 32
- Figure 7** Two-phase (liquid plus vapor) boundaries of H₂O-CH₄ fluids containing 0-4 mol% CH₄ 33
- Figure 8** The slopes of iso-T_h lines ($\Delta P/\Delta T$) as a function of homogenization temperature (T_h) calculated from equation (4) 34
- Figure 9** Iso-T_h lines for 0, 0.5, 1, 2, 3 and 4 mol% H₂O-CH₄ fluids based on the experimental results from this study 35

Chapter 3

- Figure 1** Phase behavior of a representative H₂O-CH₄ synthetic inclusion during the hydrate formation and dissociation 64
- Figure 2** Structure of the pressure cell used for Raman analysis 65
- Figure 3** An example of simultaneously collected CH₄ and Neon Raman spectra 66
- Figure 4** Raman spectra of methane hydrate at different temperatures 67
- Figure 5** Comparison of the relationship between CH₄ Raman peak position and pressure reported in different studies 68
- Figure 6** Pressure and temperature effect on methane Raman peak position between 0.3 to 22°C, 1 to 300 bars 69
- Figure 7** Change of CH₄ Raman peak position with the change of density of CH₄ as temperature drops from 295K to 270K in the pressure range of 5-200 bars ... 70
- Figure 8** P-T stability limits of methane hydrate determined from the hydrate final melting conditions of 17 synthetic fluid inclusions, in comparison with data from theoretical models and some of experimental data from previous research 71
- Figure 9** P-T stability limits of methane hydrate determined at the H-V-L_w and/or H-V-I equilibria of 4 synthetic fluid inclusions, in comparison with data from theoretical models and some of experimental data from previous research 72

Chapter 4

- Figure 1** CH₄ peak collected together with Neon peaks 86

Figure 2 Pressure and temperature dependence of the Raman CH ₄ C-H symmetric stretching band at 1°, 8°, 16° and 22°C	87
Figure 3 Change of CH ₄ Raman peak position with the change of density of CH ₄ as temperature drops from 295K to 270K in the pressure range of 5-200 bars ...	88
Figure 4 Sample configuration for the two (left) and three (right) CH ₄ molecules considered in the calculations	89
Figure 5 Sample configurations illustrating the two modes of vibration for the ν_1 symmetric vibrational stretch between two CH ₄ molecules	90

Chapter 1

Introduction

The system H₂O-CH₄ has been found in a variety of geological environments in the earth's crust, from sedimentary basins to low grade metamorphic terrains. Methane occurs in two main forms in the earth's crust. One is as a dissolved component in H₂O-CH₄ fluids associated with diagenesis and low grade metamorphism. The other is as a gas trapped as methane hydrate that occurs in the continental margins and in permafrost regions on earth. H₂O-CH₄ fluids mainly exist in natural gas fields, coal mines, and low grade metamorphic environments, at temperatures of several hundred degrees Celsius and pressures of hundreds to thousands of bars. Natural H₂O-CH₄ inclusions are evidence of the H₂O-CH₄ fluids occurring in these environments. Knowledge of the Pressure-Volume-Temperature-Composition (PVTX) properties of H₂O-CH₄ fluid inclusions, therefore, can provide information about the fluids at the inclusion trapping conditions, and also help to understand of the geological processes in which the fluids have been involved. Methane hydrate represents a huge potential energy resource. The amount of energy contained in methane hydrate world-wide has been estimated to exceed the sum of the other fossil fuels. Catastrophic dissociation of methane hydrate has also been associated with past and current climate change, and may be related to the navigation safety of sea-going ships. Methane hydrate is stable at low temperatures (less than a few tens of degrees Celsius) and moderate to high pressure (a few to hundreds or thousands of bars). Hydrate deposits have been found naturally occurring along continental margins and permafrost regions on the earth. To utilize this huge potential energy resource, it is

critical to know the pressure and temperature stability limits of methane hydrate. Although much research has been done to reach this goal, and the hydrate stability limits have been well defined, conventional methods involve significant amount of experimental time (usually up to several weeks). A faster method may not be needed for the pure methane hydrate system, but will be helpful when more complexities, such as salinity and other gas species, are added to the system.

Chapter 2 presents the results of a study of the PVTX properties of H₂O-CH₄ fluids up to 500°C, 3 kilobars at $X_{\text{CH}_4} \leq 4\text{mol}\%$ using synthetic fluid inclusions and microthermometry. The study documents the changing phase behavior of H₂O-CH₄ fluids with changing fluid composition and P-T conditions. The results of this study will be submitted to *Geochimica et Cosmochimica Acta* in October, 2005.

Chapter 3 describes a novel technique to combine synthetic fluid inclusions, microthermometry and Raman spectroscopy to study the P-T stability limits of methane hydrate. Results of this study will be submitted to *American Mineralogist* in October, 2005.

Chapter 4 addresses the shift in the Raman peak position of CH₄ gas as a function of pressure and temperature from the molecular level. The change in bond length associated with a change of fluid density, i.e., change of interaction strength between molecules, was invoked to explain the experimentally observed trend. Results of this study will be submitted to *Science* in October, 2005.

Chapter 2

Experimental determination of the PVTX properties of H₂O-CH₄ to 500°C, 3 kbars and X_{CH₄} ≤ 4 mol%

Fang Lin and R. J. Bodnar
Fluids Research Laboratory, Department of Geosciences
Virginia Polytechnic Institute and State University, Blacksburg, Virginia 24061, USA

Abstract: The Pressure-Volume-Temperature-Composition (PVTX) properties of H₂O-CH₄ were determined from the bubble point curve to 500°C and 3 kbars for compositions ≤ 4 mol% CH₄ using the synthetic fluid inclusion technique. H₂O-CH₄ inclusions were produced by loading known amounts of Al₃C₄ and H₂O into platinum capsules along with pre-fractured and inclusion-free quartz cores. During heating the Al₃C₄ and H₂O react to produce CH₄, and the H₂O-CH₄ homogeneous mixture was trapped as inclusions during fracture healing at elevated temperature and pressure. The composition of the fluid in the inclusion was confirmed by weight loss after the experiment and by Raman spectroscopic analysis of the inclusions.

Homogenization temperatures of the inclusions were determined and the results were used to construct iso-T_h lines, defined as a line connecting the formation temperature and pressure with the homogenization temperature and pressure. The pressure in the inclusion at the homogenization temperature was calculated from the Duan et al. (1992a) equation of state (EOS). The slope of each iso-T_h line ($\Delta P/\Delta T$) was calculated and the results fitted to a polynomial equation using step-wise multiple regression analysis to determine the slope of the iso-T_h line as a function of the homogenization temperature and composition according to:

$$(\Delta P/\Delta T) = a + b \cdot m + c \cdot m^4 + d \cdot (T)^2 + e \cdot m \cdot T + f \cdot m \cdot (T)^4$$

where m is the CH₄ molality, T is the homogenization temperature in degrees Celsius, and a, b, c, d, e, f are the fitting parameters. The equation is valid from the bubble point curve to 500°C and 3 kbars for compositions ≤ 4 mol% CH₄.

1. INTRODUCTION

Methane (CH₄)-bearing fluids have been reported from a number of geologic settings, including oilfields (Dubessy et al, 2001; Hao et al, 1998), low-grade metamorphic terrains (Mullis et al., 1994), mid-ocean ridge hydrothermal systems (Kelley, 1996), and anthracite coalfields (Kisch and Van Den Kerkhof, 1991). Many CH₄-bearing fluids that occur in the earth's crust are adequately modeled by the binary H₂O-CH₄ system (Dubessy et al., 2001). Failure to recognize the presence of small amounts of methane can cause significant errors in pressures estimated from fluid inclusions (Hanor, 1980; Roedder and Bodnar, 1980; Roedder, 1984).

Over the past half century, several workers have investigated the phase equilibrium properties of H₂O-CH₄ under various conditions. Culberson and McKetta (1951), Price (1979) and Ashmyan et al. (1985) report experimental data on solubility of CH₄ in water. Krader and Franck (1986) determined the high temperature boundary between the one-phase (liquid or vapor) and two-phase (liquid plus vapor) fields for two compositions in the H₂O-CH₄ system, and Jacobs and Kerrick (1981) and Saxena and Fei (1988) developed thermodynamically-based equations of state for the system. However, there are relatively few experimental studies of the volumetric (PVTX) properties of H₂O-CH₄ at elevated temperatures and pressures. Welsh (1973) studied the

H₂O-CH₄ system to 200°C and 10 kbars for compositions between 4 and 85 mol% CH₄. Zhang and Frantz (1992) studied compositions between 5.5 and 16.5 mol% CH₄ at 400 to 600°C and 1-3 kbars. The present study focuses on the lower CH₄ concentration range (0-4 mol% CH₄) at moderate temperature and pressure, because many fluids from sedimentary basins and low grade metamorphic environments contain only a few mol% CH₄ (Mullis et al., 1994; Guillaume et al., 2003).

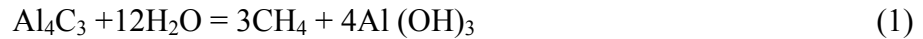
2. EXPERIMENTAL METHODS

2.1 Starting Materials and Sample Preparation

Synthetic H₂O-CH₄ fluid inclusions were produced using the synthetic fluid inclusion technique introduced by Sterner and Bodnar (1984), Bodnar and Sterner (1987) and Bodnar (1995), with minor modifications described below. Quartz cores, approximately 4 mm in diameter and 5-10 mm long, or 2mm x 3mm x 5mm quartz prisms were cut from inclusion-free Brazilian quartz. The quartz cores and prisms were cleaned by first soaking in 30% H₂O₂ solution, followed by 2M HNO₃ solution and finally boiling in doubly-distilled H₂O to remove organic, heavy metal and other contaminants that may have been introduced to the surface of the quartz cores and prisms during cutting. After cleaning, the quartz cores and prisms were heated at 350°C for 3-4 hours. The quartz cores and prisms were removed from the oven and immediately dropped into cool doubly-distilled H₂O. The thermal shock produced numerous microfractures in the quartz cores and prisms that serve as the sites of inclusion formation as the fractures heal during later hydrothermal experiments. After fracturing, the quartz

was placed into a vacuum oven at approximately 125°C to remove any water that might have entered the fractures during the fracturing event.

Hydrothermal experiments to trap H₂O-CH₄ inclusions were conducted in cold-seal vessels. Platinum capsules containing the starting materials were prepared in the following manner. First, a known amount of aluminum carbide (Al₄C₃), 20-30mg fused silica glass powder, a fractured quartz core or prism, and a known amount of distilled and deionized water were loaded into a platinum capsule (~5 mm i.d. and 25-35 mm long). Silica glass powder was added to enhance the solubility of SiO₂ in the solution to promote fracture healing. Aluminum carbide served as the source of CH₄, based upon the following reaction:



The amounts of Al₄C₃ and H₂O required were determined based on the desired final CH₄ concentration and were calculated using the reaction stoichiometry in equation (1). After all components were loaded, the capsule was sealed with a Pt end cap using cold arc welding.

After cleaning and weighing, sealed Pt capsules containing various, known CH₄ concentrations were placed into horizontally-mounted cold-seal hydrothermal vessels to trap synthetic fluid inclusions. The synthetic fluid inclusions were formed at 300° - 700°C and 1, 3 and 5 kbars to assure trapping conditions in the single-fluid-phase field. Pressure was monitored using a Bourdon-type Heise gauge and is considered to be accurate to within 50-100 bars. Temperatures, measured using chromel-alumel thermocouples, are

accurate to $\pm 3^{\circ}\text{C}$. The capsules were quenched at the end of the run (usually 5-40 days) by removing the vessels from the furnaces and allowing them to cool to room temperature. The capsules were removed from the pressure vessels, cleaned to remove any residue from the surface, dried and weighed. Capsules with equal weights before and after the run were assumed to have not leaked and were processed for analysis.

The fluid composition in the capsule at the completion of the experiment (and, presumably, in the fluid inclusions) was confirmed by comparing the fluid composition in the capsule at the end of the run to the expected composition based on the amount of water and aluminum carbide originally loaded into the capsule. The fluid composition in the capsule at the completion of the run was determined in the following manner, modified from that of Schmidt and Bodnar (2000). The cleaned capsule was wrapped with 8-fold Kimwipe tissue paper and placed into a small glass vial. A sharpened stainless steel needle was also placed in the glass vial. The weight of the entire assembly, consisting of glass vial + tissue + capsule + needle was recorded at room temperature. Next, the Pt capsule was carefully punctured by pushing the needle through the tissue and into the platinum capsule. A hissing sound was heard when the capsule was punctured and gas escaped. The tissue around the needle trapped any solid material that escaped from the capsule during puncturing, and absorbed the liquid water that was expelled from the capsule. Immediately after puncturing the capsule, the entire assembly was weighed again. The weight loss recorded at this stage represents CH_4 gas lost from the capsule as a result of opening. The amount of CH_4 remaining in the capsule dissolved in the water at room temperature and pressure is negligible, considering the solubility of CH_4 in water at 25°C and 1 bar is only about 20 ppm (cf. Duan et al., 1992b). After determining the amount of gas loss, the

assembly was placed into a vacuum oven and heated at 120°C to evaporate the water that was absorbed by the tissue and water that remained in the capsule after piercing. After approximately 5-10 hours, the assembly was removed from the oven, cooled to room temperature, and weighed again. The difference in weight between this step and that measured immediately after piercing should represent the mass of the H₂O in the capsule. We found that the Kimwipe tissue devolatilizes during heating and contributes a small amount (usually 0.005-0.02g) to the weight difference attributed to H₂O. Therefore, a control assembly, consisting of glass vial + tissue + needle, was put into the oven together with each batch of capsules. The weight loss experienced by the control assembly was subtracted from the weight loss for the experimental capsules to determine the mass of H₂O in the capsule during the experiment (and after puncturing). The composition of the H₂O-CH₄ fluid inclusion was then calculated from the measured weights of CH₄ and H₂O in the capsule. If the composition determined by weight loss did not agree within experimental error (± 0.3 mol% CH₄) with the composition based on the amounts of components originally loaded into the capsule, the sample was discarded. If the composition calculated from the amount of aluminum carbide and water originally loaded into the capsule (based the reaction stoichiometry indicated by equation 1) and post-run weight loss measurements agreed, the quartz core was processed in preparation for microthermometry analysis. A comparison of the measured and predicted compositions for the samples used for PVTX determinations are shown on Fig.1.

Two issues related to the use of aluminum carbide as the source of methane for high temperature experiments were identified during the course of this study. The first concerns the freshness of the aluminum carbide. Al₄C₃ undergoes photochemical

decomposition when exposed to light, and can slowly decompose when exposed to moisture at room temperature. The initial calibration experiments for this study used aluminum carbide from a bottle that had been opened and used previously in another study. The amounts of CH₄ generated by the Al₄C₃ - H₂O reaction were about 1/3 of the predicted amounts (Fig. 2a-d), and the measured and predicted CH₄ concentrations differed by 60-80%. In contrast, a second calibration experiment conducted under the same condition (150°C, 1 atm. external pressure) as the previous experiment but using a new batch of Al₄C₃ that had been sealed under argon by the manufacturer (Sigma-Aldrich Inc.), generated essentially identical measured and predicted compositions (Fig. 2e-h). The difference in measured and predicted compositions agreed within 12% for concentrations between 3 and 5 mol%, and within 5% for CH₄ concentrations lower than 3 mol%. Based on these results, all of the samples used in this study were prepared with aluminum carbide taken from containers immediately after breaking the manufacturer's seal and loaded directly into platinum capsules. After each capsule loading event (usually involving 10-20 capsules) the remaining aluminum carbide was discarded and a new bottle used for each new batch of capsules.

The second issue related to the aluminum carbide starting material concerns the reaction stoichiometry. Chou et al. (2001) used Al₃C₄ to generate CH₄ gas in their experiments, but they described the reaction of aluminum carbide with water as:

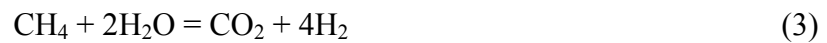


Initially, the reaction stoichiometry suggested by Chou et al. (2001) was used to determine our predicted methane concentration, but this did not produce satisfactory results. In an attempt to identify the cause of this discrepancy we conducted X-ray powder diffraction analysis of the reaction products from experiments conducted at 150°C and 1 atm. The results confirmed that the solid remaining in the capsule after the reaction of aluminum carbide with water is Al(OH)₃ (Fig. 3). Other workers have shown that aluminum hydroxides can dehydrate into aluminum oxides at elevated temperatures (Paglia, 2004). However, those studies were conducted under dry “melt” conditions, i.e., the aluminum phase was not saturated with H₂O vapor.

Comparison of CH₄ concentrations calculated using the two different reaction stoichiometries shows that the difference in calculated CH₄ concentration is small for compositions less than about 4 mol% CH₄ (Fig. 4), which is the upper composition limit for this study. However, uncertainties in the reaction stoichiometry can lead to significant errors for CH₄ concentrations higher than 4 mol%. It should also be noted that the study of Chou et al. (2001) did not require a known or controlled concentration – the only requirement was that the analytical volume contained both water and methane. Thus the uncertainty in reaction stoichiometry should not affect their results.

2.2 Effect of Formation Conditions on Fluid Composition

Depending on the oxidation state and the temperature and pressure, CH₄ may react with H₂O and produce CO₂ and H₂ (Zhang and Frantz, 1992; Murphy and Roberts, 1997; Lamb et al., 2002) according to the following reaction:



Some workers have taken steps to minimize this problem, such as using thick-wall gold capsules (Zhang and Frantz, 1992; Lamb et al., 1996; 2002), and/or using CH₄ as the pressure medium to reduce the oxygen fugacity in the cold-seal pressure vessel (Lamb et al., 1996; 2002). In this study the samples were run in platinum capsules, water was used as the pressure medium, and the pressure vessels are constructed from high-Ni alloy. Thus, in our experiments the conditions in the pressure vessel were more oxidizing than in the experiments of Zhang and Frantz (1992) and Lamb et al (1996, 2002).

All samples from this study were analyzed by Raman spectroscopy to confirm the presence of CH₄ and determine concentrations of other volatiles. During the analyses, CO₂ was detected in all fluid inclusions trapped at and above 600°C (Fig. 5). In fluid inclusions trapped at 500°C, CO₂ was only detected in inclusions containing greater than 5 mol% CH₄ (Fig. 5). The failure to detect CO₂ in inclusions with less than 5 mol% CH₄ is believed to reflect lower internal pressures of these inclusions, and not necessarily a lower CO₂/CH₄ fraction in the gas phase. The detection limit of a gas species in a fluid inclusion is determined by the partial pressure of the species in the inclusion, and not its bulk concentration (Wopenka and Pasteris, 1987). No CO₂ was detected in fluid inclusions trapped at 300 and 400°C (Fig. 5). No relationship was observed between the presence of CO₂ and the trapping pressure of the inclusions. A significantly greater mass of gas (compared to the predicted mass assuming only CH₄) was released from those capsules containing samples that later showed CO₂ in the inclusions, similar to observations by Lamb et al (2002). Based on previous work in this laboratory (Rosso and Bodnar, 1995), the detection limit for CO₂ in fluid inclusions is less than 1 bar. As the total pressure in most inclusions from this study is in the range of several tens to

hundreds of bars, the partial pressure (and concentration) of CO₂ is thought to be insignificant in all inclusions trapped at $\leq 500^{\circ}\text{C}$.

According to equation (3), hydrogen gas is also produced by the reaction to produce CO₂. However, H₂ gas was not detected in any of the inclusions synthesized in this study. This is not surprising as it is well known that hydrogen diffuses easily through platinum at elevated temperatures (Chou, 1986), and H₂ is easily lost from fluid inclusions during modest heating (Mavrogenes and Bodnar, 1994).

2.3. Microthermometric Analysis

Samples containing synthetic H₂O-CH₄ inclusions were placed into a FLUID INC-adapted USGS gas-flow heating/cooling stage for microthermometry analysis. The thermocouple was calibrated at 0.0 and 374.1°C using pure water synthetic fluid inclusions. The accuracy in the temperature range in which fluid inclusions from this study homogenized is $\pm 1^{\circ}\text{C}$ (Sterner and Bodnar, 1984). Homogenization temperatures (denoted as T_h hereafter) of 5-37 inclusions were measured in each sample, each representing a unique P-T-X formation condition. Fewer measurable inclusions ($\geq 5 \mu\text{m}$) were found in samples formed at lower temperatures (300°C) compared to samples run at higher temperature. Inclusions of different size and shape and from different locations within the sample were analyzed. Only those samples that showed consistent T_h data were included in the final dataset.

3. RESULTS AND DISCUSSION

All inclusions produced in this study contained two phases (an aqueous liquid phase and a CH₄-rich gas phase) when observed at room temperature. The single exception is sample 070605-1, formed at 300°C and 3 kbar and containing pure H₂O, which contained metastable 1-phase liquid inclusions together with the more common 2-phase liquid plus vapor inclusions. Such single-phase, metastable inclusions are common in samples formed at high pressure, low temperature conditions (Roedder, 1971, Invernizzi et al., 1998). Upon heating, all the 2-phase inclusions from all samples homogenized into the liquid aqueous phase, indicating that all the fluid inclusions trapped a single liquid phase at formation conditions.

The mean T_h of fluid inclusions from each sample increases systematically with increasing CH₄ concentrations (Fig. 6). The relationship between mean T_h and CH₄ concentration is adequately described by second order polynomial equations for experiments run at 300°C, 400°C and 500°C. Noticeably, pure H₂O samples generated T_h values equivalent ($\pm 3^\circ\text{C}$) to those predicted from the water steam tables (Haar et al., 1984) as was observed previously by Bodnar and Sterner (1985).

The goal of this study was to produce internally consistent experimental data that could be used to interpret microthermometric results from fluid inclusions containing low CH₄ concentrations (≤ 4 mol%). When fluid inclusions are trapped in the one-phase field, it is necessary to know the temperature of homogenization, the pressure inside the inclusion at homogenization, and the slope of the isochore in P-T space, in order to estimate a pressure correction and determine a trapping temperature (Roedder and Bodnar, 1980). Isochores represent lines of constant density or volume and, to a first approximation, fluid inclusions represent isochoric systems. However, owing to the small

change in volume due to thermal expansion and compressibility of the host mineral, fluid inclusions are not truly isochoric (see Bodnar and Sterner, 1985; Sterner and Bodnar, 1991). For this reason, many workers now prefer to use iso- T_h lines as these more accurately reflect the P-T paths that fluid inclusions follow in P-T space (Bodnar and Vityk, 1994; Schmidt et al., 1995; Bodnar, 2003a). The non-isochoricity of each iso- T_h line is listed in Table 2.

In this study, a straight line connecting the temperature and pressure of formation of the inclusion and the temperature and pressure at homogenization represents an iso- T_h line. The temperature and pressure of formation are known for each inclusion from the experimental conditions, and the homogenization temperature is known from microthermometric analysis of the inclusions, requiring only the pressure inside the inclusion at homogenization to calculate the iso- T_h line. All of the inclusions in this study homogenize along the bubble point curve separating the two-phase (liquid plus vapor) field from the single-phase liquid field. While the pressure in the inclusion at the moment of homogenization cannot be measured directly, it can be calculated from the known homogenization temperature and fluid composition using an appropriate equation of state. Phase boundaries for 0, 0.5, 1, 2, 3, and 4 mol% CH_4 compositions, calculated from the equation of state of Duan et al. (1992a), are shown on Figure 7. The Duan et al. (1992a) equation was used to determine the pressure in the fluid inclusions at homogenization.

The slope of the iso- T_h line was calculated for each of the 49 samples in this study. The results are listed in Table 2. The data were then analyzed using a step-wise multiple regression algorithm to determine a relationship between the slope of the iso- T_h lines and the composition and homogenization temperature according to:

$$(\Delta P/\Delta T) = a + b \cdot m + c \cdot m^4 + d \cdot (T)^2 + e \cdot m \cdot T + f \cdot m \cdot (T)^4 \quad (4)$$

where m is the CH₄ molality, T is the homogenization temperature in degrees Celsius, and a, b, c, d, e, f are the fitting parameters (Table 3). R^2 value of the fitted equation is 0.9153, indicating a good fitting of equation (4) with the experimental data. The equation is valid from the bubble point curve up to 500°C and 3 kbars for compositions ≤ 4 mol% CH₄.

The slopes of iso- T_h lines ($\Delta P/\Delta T$) as a function of homogenization temperature and composition for 0, 0.5, 1, 2, 3, and 4 mol% CH₄ are shown in Fig. 8. The slopes of all iso- T_h lines decrease with increasing temperature, as expected. Note that at low temperatures (<300°C) the slopes of CH₄-bearing compositions are steeper than that of pure H₂O (i.e., the CH₄-bearing fluids are less compressible than H₂O). At higher temperatures the CH₄-bearing fluids are slightly more compressible than H₂O (slopes are less steep). The lowest T_h value shown for each composition corresponds to either 125°C or the temperature corresponding to a pressure of 3 kbars on the bubble point curve for that composition.

Using equation (4), iso- T_h lines have been calculated in increments of 20°C for six compositions between 0 and 4 mol% CH₄ and the results are plotted in Fig. 9. The highest temperature and pressure of the experiments is 500°C and 3 kbar, and these empirical iso- T_h lines should not be extrapolated beyond these limits. It should be noted that the pressures along the bubble-point curve shown in Fig. 9 extend to >1 kbar for several of the compositions. In practice, many fluid inclusions in quartz will stretch or

decrepitate if the internal pressure exceeds about 1 kbar during heating (Bodnar et al., 1989; Bodnar, 2003b)

4. Summary

The synthetic fluid inclusion technique has been used to determine the PVTX properties of H₂O-CH₄ from the bubble point curve to 500°C and 3 kbars for compositions ≤ 4 mol% CH₄. Methane in the experiments was generated by the reaction of H₂O with aluminum carbide (Al₃C₄). Because the aluminum carbide decomposes when exposed to light or moisture, care must be taken to use only fresh material when preparing samples. Additionally, above 500°C methane will react with water to produce carbon dioxide plus hydrogen at oxygen fugacities controlled by the Ni-NiO buffer. Thus, experiments in the H₂O-CH₄ system should be conducted at reduced oxidation states (more reducing than Ni-NiO) and/or at temperatures $\leq 500^\circ\text{C}$. Additionally, owing to uncertainties concerning the stoichiometry of the Al₃C₄-H₂O reaction, the final composition should be measured independently to confirm the calculated composition. The relative error in CH₄ concentration increases with increasing CH₄. Over the range of compositions investigated here ($X_{\text{CH}_4} \leq 0.04$) the error resulting from uncertainty in the reaction stoichiometry is insignificant.

Microthermometric data obtained from synthetic fluid inclusions trapped at 300 - 500°C, 1-3 kilobars and containing ≤ 4 mol% CH₄ were used to determine the relationship between the slope of lines of constant homogenization temperature (iso-T_h lines) and homogenization temperature and composition. The slope ($\Delta P/\Delta T$) decreases systematically with increasing T_h for all compositions. At temperatures below about

300°C the slopes of iso- T_h lines increase with increasing CH_4 concentration. The trend is reversed at higher temperatures. The slopes of iso- T_h lines were analyzed using a step-wise multiple regression technique to obtain an empirical relationship between the slope and the homogenization temperature and composition. The resulting algorithm is valid from the liquid-vapor boundary to 500°C and 3 kbars for compositions ≤ 4 mol% CH_4 .

Acknowledgements— Dr. Nizhou Han provided the purified silica glass powder used in the experiments. Mr. Charles Farley assisted with hydrothermal experiments and Raman analyses, and Jin Zhao assisted with X-ray diffraction analyses in the Crystallography Laboratory at Virginia Tech. Ms. Younan Chen from the Department of Statistics at Virginia Tech provided guidance on regression analysis of the data. Comments on an earlier version of this manuscript by Drs. P. Dove, F. Read, M. Schreiber and A. Sum are greatly appreciated.

References:

- Ashmyan K.D., Skripka V.G. and Namiot Y.Y. (1985) The solubilities of methane and nitrogen in water at high temperatures and pressures. *Geokhimiya* 4, 580-581.
- Bodnar R. J. (1995) Experimental determination of the PVTX properties of aqueous solutions at elevated temperatures and pressures using synthetic fluid inclusions: H₂O-NaCl as an example. *Journal of Pure and Applied Chemistry* 67, 873-880.
- Bodnar R. J. (2003a) Introduction to aqueous fluid systems. In I. Samson, A. Anderson, & D. Marshall, eds. *Fluid Inclusions: Analysis and Interpretation*. Mineral. Assoc. Canada, Short Course 32, 81-99.
- Bodnar R. J. (2003b) Reequilibration of fluid inclusions. In I. Samson, A. Anderson, & D. Marshall, eds. *Fluid Inclusions: Analysis and Interpretation*. Mineral. Assoc. Canada, Short Course 32, 213-230.
- Bodnar R. J., Binns P. R. & Hall D. L. (1989) Synthetic fluid inclusions. VI. Quantitative evaluation of the decrepitation behavior of fluid inclusions in quartz at one atmosphere confining pressure. *Journal of Metamorphic Geology* 7, 229-242.
- Bodnar R. J. and Sterner S. M. (1985) Synthetic fluid inclusions in natural quartz. II. Application to PVT studies. *Geochimica et Cosmochimica Acta* 49, 1855-1859.
- Bodnar R. J. and Sterner S. M. (1987) Synthetic fluid inclusions: Hydrothermal Experimental Techniques (G.C. Ulmer and H.L. Barnes, eds.). Wiley-Interscience, New York, p. 423 – 457.
- Bodnar R. J. & Vityk M. O. (1994) Interpretation of microthermometric data for H₂O-NaCl fluid inclusions. in *Fluid Inclusions in Minerals, Methods and Applications*, B. De Vivo and M. L. Frezzotti, eds., pub. by Virginia Tech, Blacksburg, VA, p. 117-130.
- Chou I-M. (1986) Permeability of precious metals to hydrogen at 2 kb total pressure and elevated temperatures. *American Journal of Science* 286, 638-658.
- Chou I-M., Sharma A., Burruss R.C., Hemley R., Goncharov A.F., Stern L.A. and Kirby S.H. (2001) Diamond-anvil cell observation of a new methane hydrate phase in the 100-MPa pressure range. *Journal of Physical Chemistry A* 105, 4664-4668.
- Culberson O. L. and McKetta Jr. J. J. (1951) Phase equilibria in hydrocarbon-water system, III. The solubility of methane in water at pressures to 10,000 psi. *Journal of Petroleum Technology* 4, 223-226.
- Duan Z., Møller N. and Weare J. H. (1992a) An equation of state for the CH₄-CO₂-H₂O system: II. Mixtures from 50 to 1000°C and 0 to 1000 bar. *Geochim. et. Cosmochim. Acta* 56, 2619-2631.

- Duan Z., Møller N., Greenberg J. and Weare J. (1992b) The prediction of methane solubility in natural waters to high ionic strength from 0 to 250°C and from 0 to 1600 bars. *Geochimica et Cosmochimica Acta* 56, 1451-1460.
- Dubessy J., Buschaert S., Lamb W., Pironon J. and Thiéry R. (2001) Methane-bearing aqueous fluid inclusions: Raman analysis, thermodynamic modeling and application to petroleum basins. *Chemical Geology* 173, 193-205.
- Guillaume D., Teinturier S., Dubessy J. and Pironon J. (2003) Calibration of methane analysis by Raman spectroscopy in H₂O-NaCl-CH₄ fluid inclusions. *Chemical Geology* 194, 41-49.
- Haar L., Gallagher J. S. and Kell G. S. (1984) NBS/NBC Steam Tables. Hemisphere, 320pp.
- Hanor J. S. (1980) Dissolved methane in sedimentary brines: potential effect on the PVT properties of fluid inclusions. *Economic Geology* 75, 603-617.
- Hao F., Li S., Sun Y. and Zhang Q. (1998) Geology, compositional heterogeneities, and geochemical origin of the Yacheng gas field, Qiongdongnan Basin, South China Sea. *AAPG Bulletin* 82, 1372-1384.
- Invernizzi C., Vityk M. O., Cello G. and Bodnar, R. J. (1998) Fluid inclusions in high pressure/low temperature rocks from the Calabrian Arc (southern Italy): the burial and exhumation history of the subduction-related Diamante-Terranova unit. *Journal of Metamorphic Geology*, 16, 247-258.
- Jacobs G. K. and Kerrick D. M. (1981) Methane: an equation of state with application to the ternary system H₂O-CO₂-CH₄. *Geochimica et Cosmochimica Acta* 45, 607-614.
- Kelley D. S. (1996) Methane-bearing fluids in the oceanic crust: Gabbro-hosted fluid inclusions from the southwest Indian Ridge. *Journal of Geophysical Research* 101, 2943-2962.
- Kisch H. J. and Van Den Kerkhof A. M. (1991) CH₄-rich inclusions from quartz veins in the Valley- and Ridge province and the anthracite fields of the Pennsylvania Appalachians. *The American Mineralogist* 76, 320-340.
- Krader T. and Franck E. U. (1986) Phase equilibria and critical phenomena of the ternary system H₂O-CH₄-NaCl to 500°C and 2500 bar. *Physica B+C* 139-140, 66-69.
- Lamb W. M., Popp R. K. and Boockoff L. A. (1996) The determination of phase relations in the CH₄-H₂O-NaCl system at 1 kbar, 400 to 600°C using synthetic fluid inclusions. *Geochimica et Cosmochimica Acta* 60, 1885-1897.

- Lamb W. M., McShane C. J. and Popp R. K. (2002) Phase relations in the CH₄-H₂O-NaCl system at 2 kbar, 300 to 600°C as determined using synthetic fluid inclusions, *Geochimica et Cosmochimica Acta* 66, 3971-3986.
- Mavrogenes J. A. and Bodnar R. J. (1994) Hydrogen movement into and out of fluid inclusions in quartz: Experimental evidence and geologic implications. *Geochimica et Cosmochimica Acta* 58, 141-148.
- Mullis J., Dubessy J., Poty B. and O'Neil J. (1994) Fluid regimes during late stages of a continental collisions: Physical, chemical, and stable isotope measurements of fluid inclusions in fissure quartz from a geotraverse through the Central Alps, Switzerland, *Geochimica et Cosmochimica Acta* 58, 2239-2267.
- Murphy P. J. and Roberts S. (1997) Melting and nucleation behaviour of clathrates in multivolatile fluid inclusions: evidence of thermodynamic disequilibrium. *Chemical Geology* 135, 1-20.
- Paglia G. (2004) Determination of the Structure of γ -Alumina using Empirical and First Principles Calculations combined with Supporting Experiments. Ph.D. Thesis, Curtin University of Technology, Australia, 341pp.
- Price L. C. (1979) Aqueous solubility of methane at elevated pressures and temperatures. *AAPG Bulletin* 63, 1527-1533.
- Roedder E. (1971) Metastability in Fluid Inclusions. *Soc. Mining Geol. Japan, Spec. Issue* 3, 327-334.
- Roedder E. (1984) Fluid inclusions. *Reviews in Mineralogy*, vol.12. Mineralogical Society of America, 644pp.
- Roedder E & Bodnar R. J. (1980) Geologic pressure determinations from fluid inclusion studies. *Annual Review of Earth and Planetary Sciences*, 8, 263-301.
- Rosso K. M. & Bodnar R. J. (1995) Detection limits of CO₂ in fluid inclusions using microthermometry and laser Raman spectroscopy and the spectroscopic characterization of CO₂. *Geochimica et Cosmochimica Acta*, 59, no. 19, 3961-3975.
- Saxena S. K. and Fei Y. (1988) Fluid mixtures in the C-O-H system at high pressure and temperature. *Geochimica et Cosmochimica Acta* 52, 505-512.
- Schmidt C. & Bodnar R. J. (2000) Synthetic fluid inclusions: XVI. PVTX properties in the system H₂O-NaCl-CO₂ at elevated temperatures, pressures, and salinities. *Geochimica et Cosmochimica Acta* 64, 3853-3869.
- Schmidt C, Rosso K. M. & Bodnar R. J. (1995) Synthetic fluid inclusions. XIII: Experimental determination of the PVTX properties in the system (H₂O + 40 wt.% NaCl)

- CO₂ at elevated temperatures and pressures. *Geochimica et Cosmochimica Acta* 59, 3953-3959.

Sterner S. M. and Bodnar R. J. (1984) Synthetic fluid inclusions in natural quartz. I. Compositional types synthesized and applications to experimental geochemistry. *Geochimica et Cosmochimica Acta* 48, 2659-2668.

Sterner S. M. and Bodnar R. J. (1991) Synthetic fluid inclusions. X: Experimental determination of P-V-T-X properties in the CO₂-H₂O system to 6 kb and 700°C. *American Journal of Science* 291, 1-54.

Welsh H. (1973) Die Systeme Xenon-Wasser und Methan-Wasser bei hohen Drücken und Temperaturen. Ph.D. Thesis, Universität Karlsruhe, Karlsruhe, 41pp.

Wopenka B. and Pasteris J. D. (1987) Raman Intensities and Detection Limits of Geochemically Relevant Gas Mixtures for a Laser Raman Microprobe. *Anal. Chem.* 59, 2165-2170.

Zhang Y. and Frantz J. D. (1992) Hydrothermal reactions involving equilibrium between minerals and mixed volatiles. 2. Investigation of fluid properties in the CO₂-CH₄-H₂O system using synthetic fluid inclusions. *Chemical Geology* 100, 51-72.

Table 1. Formation condition and homogenization temperatures measured for the synthetic inclusions.

Sample ID	T _f (°C) ^a	P _f (bar) ^b	X (mol%CH ₄) ^c	Mean T _h (°C) ^d	Range (°C) ^e	N ^f	S. D. ^g
091504-1	500	1000	0	357.9	3.3	30	0.78
091504-2	500	1000	0.39	356.4	1.3	37	0.30
091504-3	500	1000	0.73	358.8	1.0	23	0.20
091504-4	500	1000	1.41	359.0	1.1	25	0.34
091504-5	500	1000	1.88	358.7	1.5	27	0.43
091504-6	500	1000	2.77	360.1	1.5	24	0.37
091504-7	500	1000	3.76	361.4	1.7	25	0.43
092604-1	500	2000	0	305.0	3.7	32	0.86
092604-2	500	2000	0.17	305.4	0.8	27	0.23
022704-1	500	2000	0.21	307.3	1.9	31	0.72
092604-4	500	2000	0.69	308.7	2.7	26	0.63
092604-3	500	2000	0.706	308.0	2.5	27	0.55
022704-2	500	2000	0.78	309.9	2.7	30	0.90
092604-5	500	2000	1.67	312.8	1.3	27	0.34
092604-6	500	2000	2.33	315.9	2.7	30	0.46
092604-7	500	2000	2.87	319.8	3.8	33	0.77
111004-1	500	3000	0	262.6	3.1	36	0.69
111004-3	500	3000	0.707	270.1	3.1	31	0.75
111004-4	500	3000	1.07	270.6	4.6	31	0.99
111004-2	500	3000	2.23	281.5	4.5	40	1.28
111004-5	500	3000	3.09	289.6	3.4	25	0.79
070705-7	400	1000	0	304.3	7.3	12	2.61
070705-8	400	1000	0.53	305.2	8.9	18	2.49
070705-10	400	1000	1.16	309.8	11.0	17	3.55
070705-12	400	1000	3.1	323.2	9.0	14	2.87
040405-5	400	1000	3.93	326.9	4.2	15	1.25
052605-1	400	2000	0	251	9.7	14	3.00
052605-2	400	2000	1.085	260.9	7.6	13	2.37
052605-3	400	2000	2.1	273.2	6.3	8	2.66
052605-4	400	2000	3.1	284.3	8.7	12	3.33
052605-5	400	2000	4.03	291.5	7.8	10	2.64
053005-1	400	3000	0	205.1	4.8	12	1.52
053005-2	400	3000	0.54	216.9	7.5	14	2.31
053005-3	400	3000	1.04	228	8.1	11	2.80
053005-4	400	3000	2.12	250.7	5.7	7	2.11
053005-5	400	3000	3.03	266	6.7	14	2.24
102104-1	300	1000	0	230.2	3.1	15	0.93
102104-2	300	1000	0.66	239.4	9.9	14	2.85
102104-3	300	1000	1.11	246.5	11.8	8	4.66
102104-4	300	1000	1.44	256.4	17.1	5	6.90

102104-5	300	1000	1.97	271.6	12.1	5	4.66
102104-6	300	1000	3.15	281.9	13.9	8	4.06
121004-11	300	2000	0	180.5	3.1	17	0.85
121004-3	300	2000	1.56	227.7	12.1	9	4.51
121004-8	300	2000	2.36	249.3	13.5	10	5.42
070605-1	300	3000	0	141.9	6.4	7	2.05
070605-2	300	3000	0.58	162.5	10.7	10	3.95
070605-3	300	3000	1.08	191.3	9.0	8	3.06
070605-4	300	3000	2.03	227.8	9.6	8	3.70

a-formation temperature

b-formation pressure

c-composition

d-arithmetic mean of the measured homogenization temperatures

e-range of the measure homogenization temperature.

f-number of measured inclusions

g-standard deviation of the measured homogenization temperatures

Table 2. Slope of iso- T_h lines calculated for each experimental composition*.

Sample ID	T_f (°C)	P_f (bars)	T_h (°C)	P_{Th} (bars) ^h	X (molality)	$\Delta V_{Th \rightarrow Tf}$ (%) ^j	$\Delta P/\Delta T$
091504-1	500	1000	357.9	183.7	0	0.71	5.75
091504-2	500	1000	356.4	194.4	0.22	0.72	5.61
091504-3	500	1000	358.8	210.4	0.41	0.71	5.59
091504-4	500	1000	359	235.1	0.79	0.72	5.42
091504-5	500	1000	358.7	252.9	1.06	0.73	5.29
091504-6	500	1000	360.1	287.7	1.58	0.74	5.09
091504-7	500	1000	361.4	326.8	2.17	0.74	4.86
092604-1	500	2000	305	92.4	0	0.54	9.78
092604-2	500	2000	305.4	109	0.09	0.55	9.72
022704-1	500	2000	307.3	114.7	0.12	0.54	9.78
092604-4	500	2000	308.7	162.5	0.39	0.55	9.61
092604-3	500	2000	308	163.9	0.39	0.55	9.56
022704-2	500	2000	309.9	171.9	0.44	0.54	9.62
092604-5	500	2000	312.8	266.5	0.94	0.56	9.26
092604-6	500	2000	315.9	339.7	1.32	0.57	9.02
092604-7	500	2000	319.8	395	1.64	0.57	8.91
111004-1	500	3000	262.6	49	0	0.38	12.43
111004-3	500	3000	270.1	174.2	0.40	0.38	12.29
111004-4	500	3000	270.6	247.4	0.60	0.40	12.00
111004-2	500	3000	281.5	487.7	1.27	0.43	11.50
111004-5	500	3000	289.6	673.1	1.77	0.45	11.06
070705-7	400	1000	304.3	91.5	0	0.22	9.49
070705-8	400	1000	305.2	144.7	0.30	0.23	9.02
070705-10	400	1000	309.8	211.9	0.65	0.23	8.74
070705-12	400	1000	323.2	409.5	1.78	0.23	7.69
040405-5	400	1000	326.9	498.4	2.27	0.24	6.86
052605-1	400	2000	251	40.5	0	0.13	13.15
052605-2	400	2000	260.9	275.3	0.61	0.16	12.40
052605-3	400	2000	273.2	512.4	1.19	0.18	11.73
052605-4	400	2000	284.3	752.1	1.77	0.20	10.79
052605-5	400	2000	291.5	1048.1	2.33	0.26	8.77
053005-1	400	3000	205.1	17.3	0	0.05	15.30
053005-2	400	3000	216.9	206.7	0.30	0.05	15.26
053005-3	400	3000	228	398.5	0.58	0.05	15.13
053005-4	400	3000	250.7	795.2	1.20	0.06	14.77
053005-5	400	3000	266	1129.9	1.73	0.09	13.96
102104-1	300	1000	230.2	28.1	0	0.04	13.92
102104-2	300	1000	239.4	204.3	0.37	0.05	13.13
102104-3	300	1000	246.5	334	0.62	0.05	12.45
102104-4	300	1000	256.4	402.4	0.81	0.03	13.71
102104-5	300	1000	271.6	482.1	1.12	-0.03	18.24

102104-6	300	1000	281.9	814.6	1.80	0.03	10.24
121004-11	300	2000	180.5	10.3	0	-0.03	16.65
121004-3	300	2000	227.7	752.4	0.88	-0.03	17.26
121004-8	300	2000	249.3	1019	1.34	-0.05	19.35
070605-1	300	3000	141.9	3.9	0	-0.13	18.95
070605-2	300	3000	162.5	468.4	0.32	-0.09	18.41
070605-3	300	3000	191.3	830.3	0.61	-0.12	19.96
070605-4	300	3000	227.8	1333	1.15	-0.14	23.09

* please see the footnote of Table 1 for most symbols used in this table

h-pressure on the liquid vapor curve at the correspondent homogenization temperature

j-non-isochoricity, represented by the volume change of an inclusion from its formation condition to homogenization condition (in percentage)

Table 3. Fitting parameters for equation (4).

Fitting Parameters	
a	19.53860
b	30.49833
c	-1.859E-2
d	-1.0733E-4
e	-1.2478E-1
f	8.56213E-10

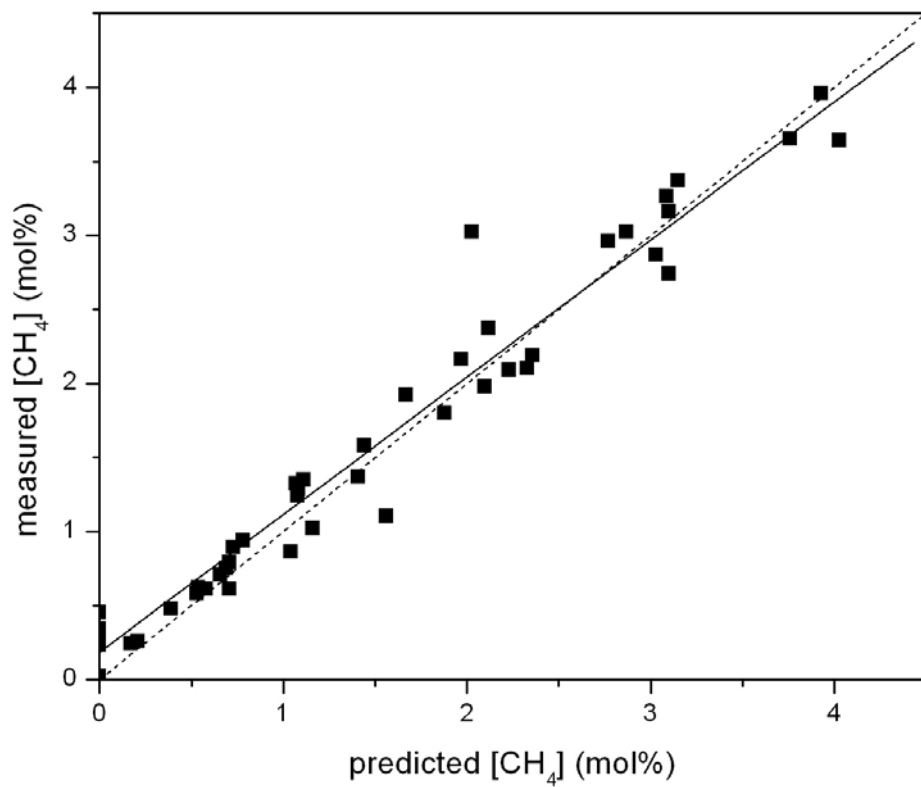


Figure 1. Comparison of the predicted versus measured CH₄ concentration of the synthetic fluid inclusions. The short dash line represents the 1:1 correlation line. The solid line represents the linear fit line for the experimental data.

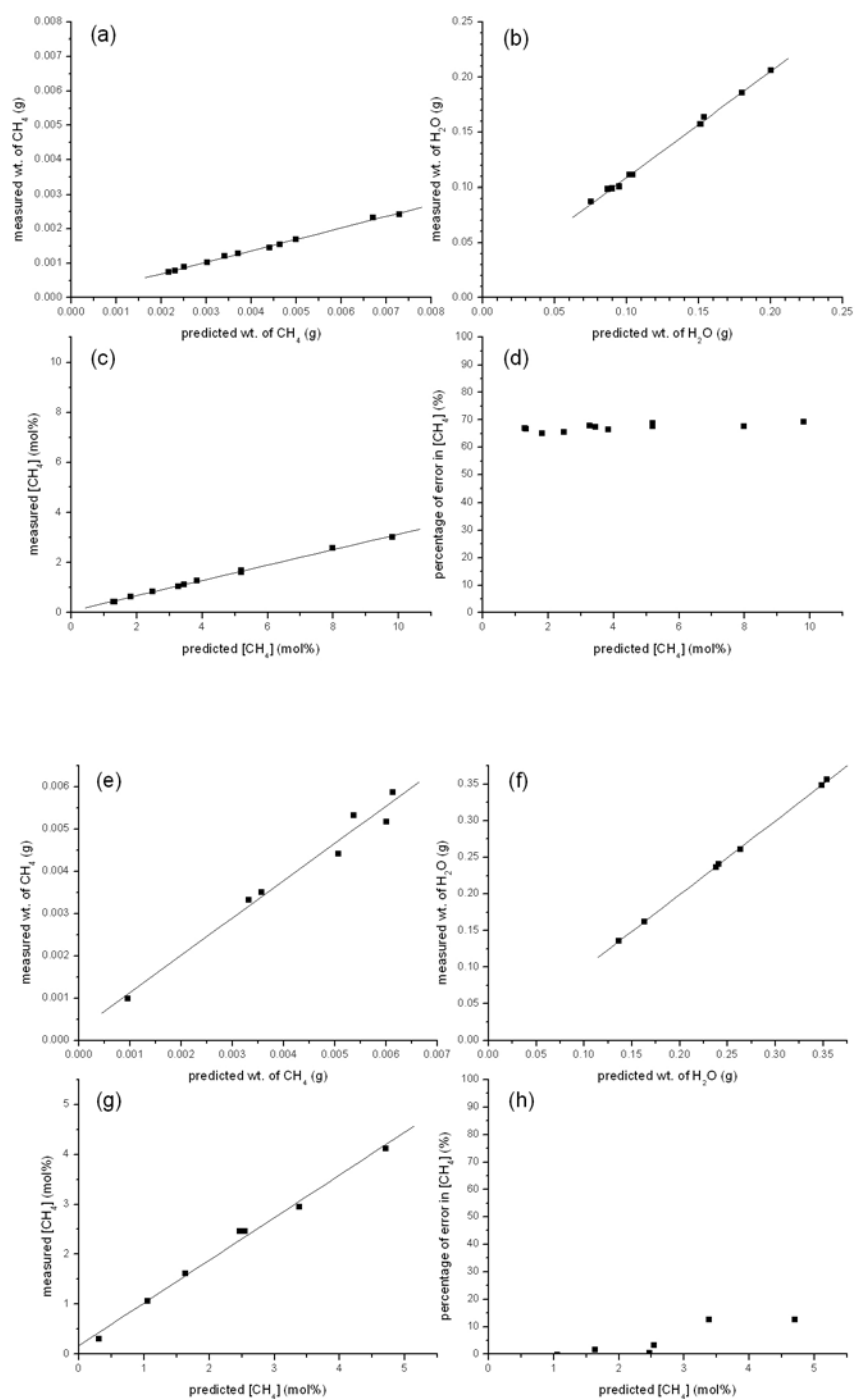


Figure 2. Comparison of the predicted versus measured CH_4 concentration produced using older (a-d) and fresh (e-h) Al_3C_4 to generate CH_4 . Both sets of experiments were conducted at 150°C , 1 atm external pressure. The solid lines are the trend lines fit to the data by linear regression.

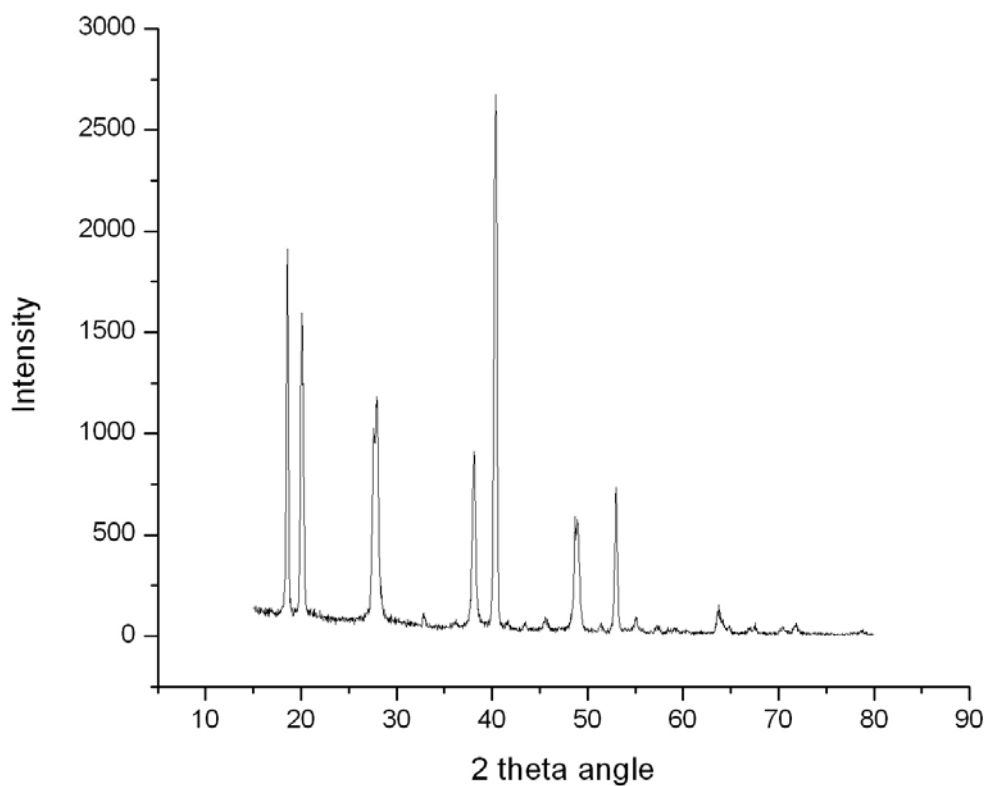


Figure 3. X-ray powder diffraction pattern of the solid material remaining in the capsule at the end of an experiment. The residual was collected from experiment 092203 conducted at 150°C, 1 atm external pressure. The analysis was conducted using a Scintag X-ray powder diffractometer with $\text{CuK}\alpha$ radiation (1.54Å wavelength). The resulting diffraction pattern confirms that the solid material is $\text{Al}(\text{OH})_3$.

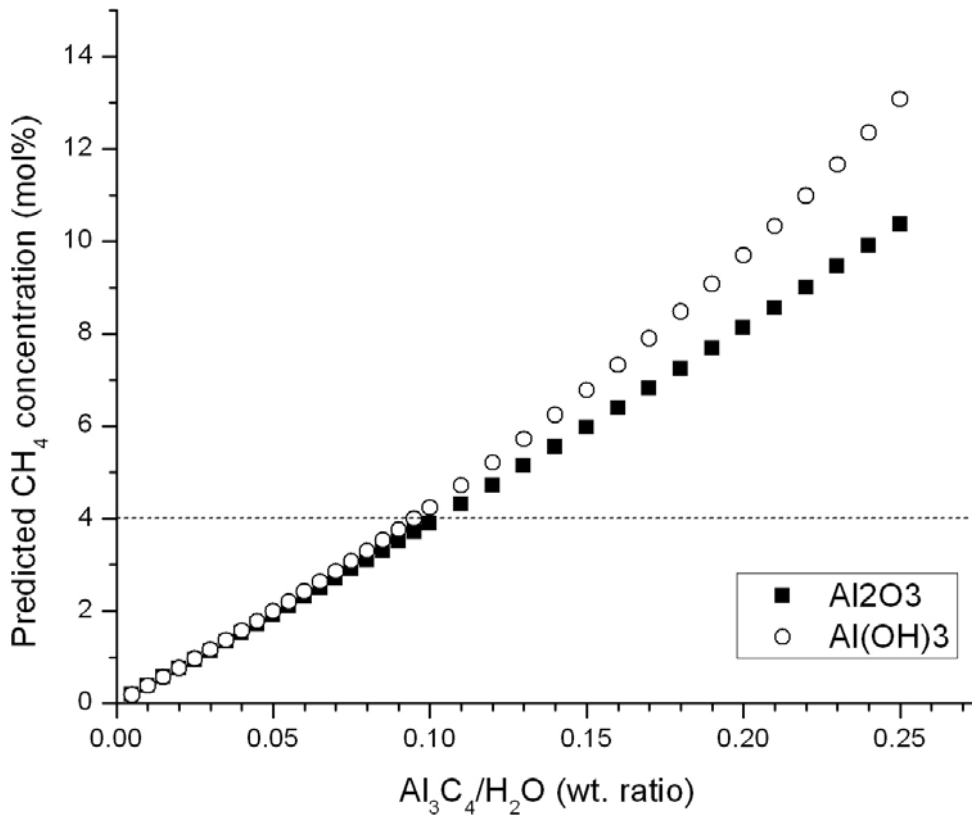


Figure 4. Comparison of the effect of assumed reaction stoichiometry on the predicted composition of H₂O-CH₄ fluids generated by the Al₃C₄ - H₂O reaction. In this study, all compositions were ≤ 4mol% CH₄ (see horizontal dash line).

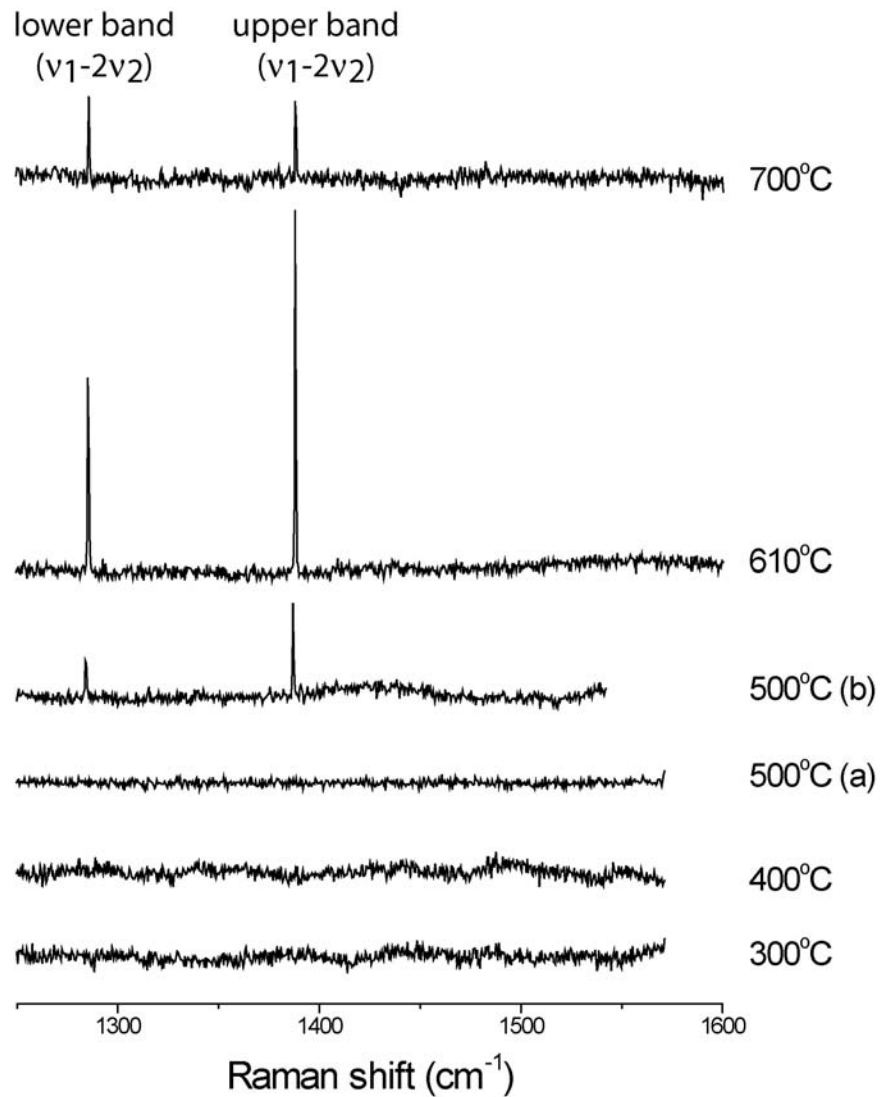


Figure 5. Raman spectra of the synthetic fluid inclusions trapped at various temperatures from 300° to 700°C. The Fermi diad of CO₂ gas around 1285 cm⁻¹ and 1388 cm⁻¹ confirms the presence of carbon dioxide in the inclusions. Carbon dioxide was not detected in inclusions trapped at 300°, 400° or at 500°C and containing <5 mol% CH₄ (spectrum labeled “500°C a”), but was found in inclusions trapped at 500°C and containing >5 mol% CH₄ (spectrum labeled “500°C (b)”) and in the inclusions formed at 610° and 700°C.

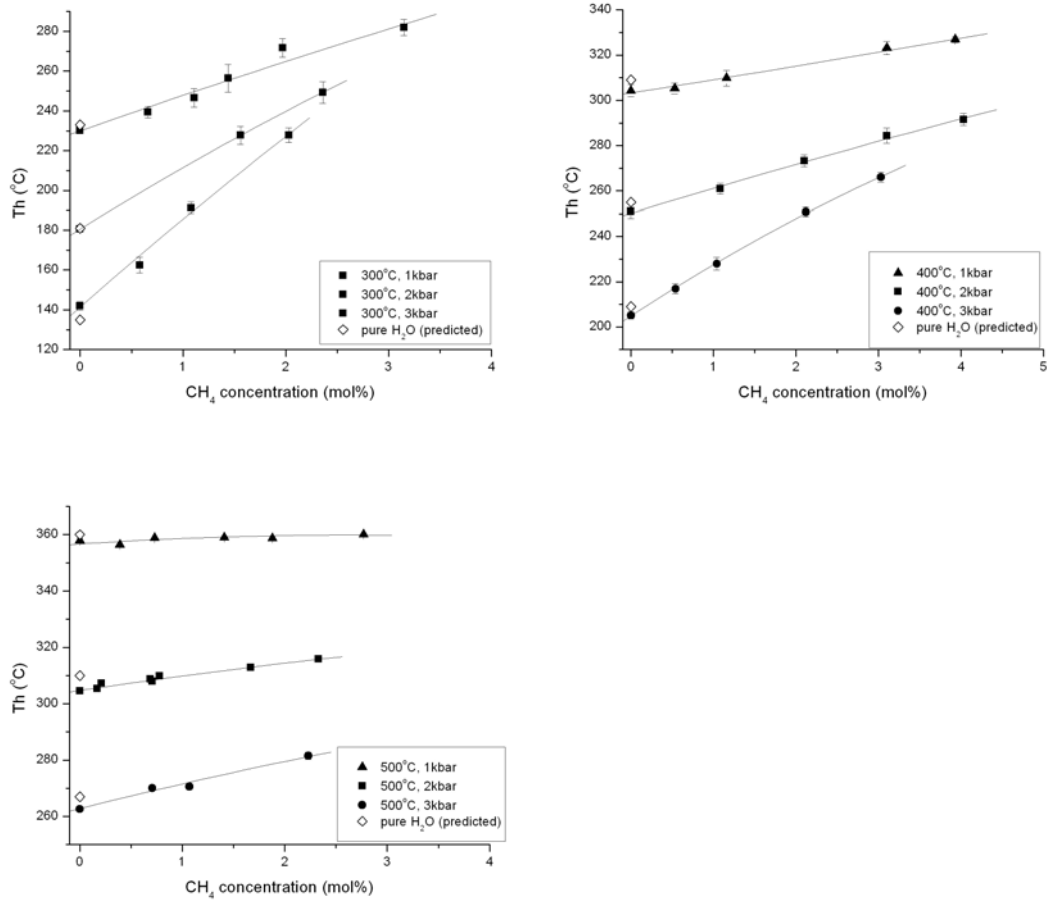


Figure 6. Relationship between homogenization temperature (T_h) and CH_4 concentration for inclusions trapped at 300°C, 400°C and 500°C and pressures of 1-3 kbars. Error bars represent the standard deviation of the T_h values for that sample. In each sample, 5-37 inclusions were measured.

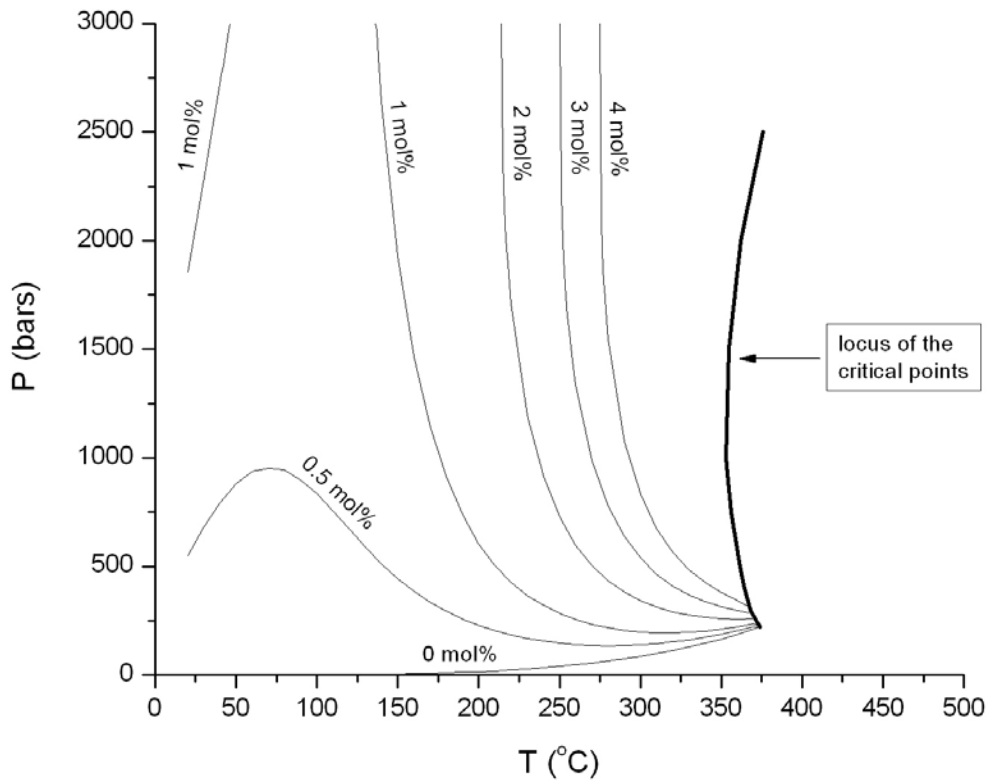


Figure 7. Two-phase (liquid plus vapor) boundaries of H₂O-CH₄ fluids containing 0-4 mol% CH₄. The phase boundaries were calculated using the Duan et al. (1992a) equation of state. Data for the locus of critical points are from Welsh (1978).

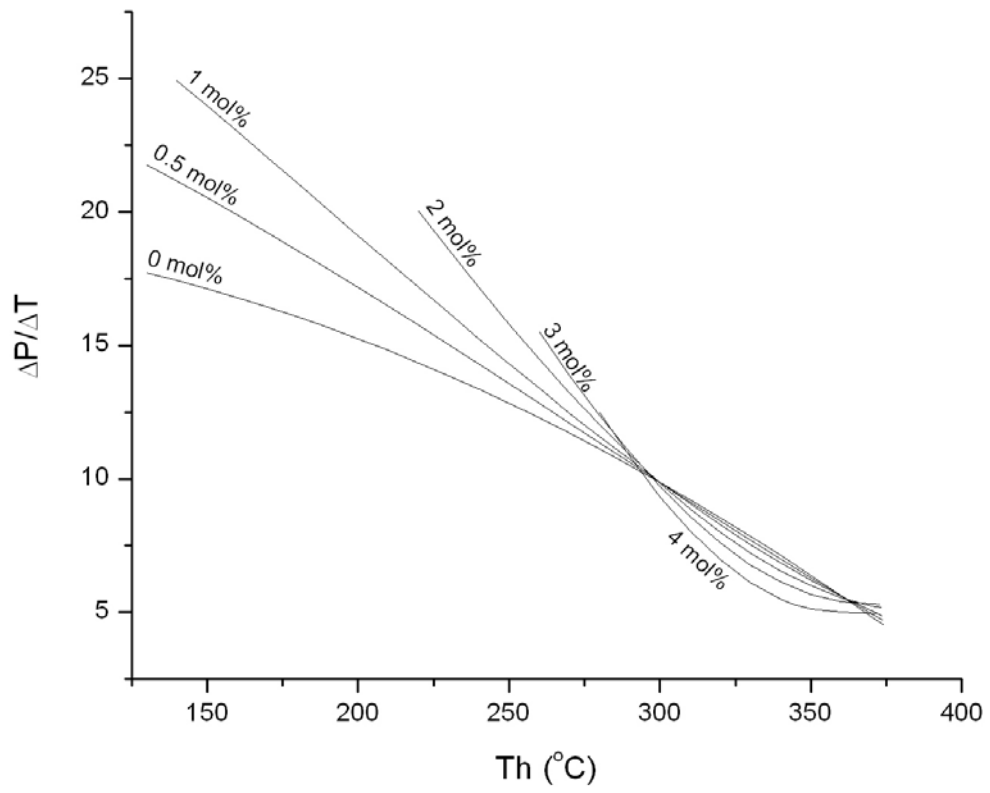


Figure 8. The slopes of iso- T_h lines ($\Delta P/\Delta T$) as a function of homogenization temperature (T_h) calculated from equation (4).

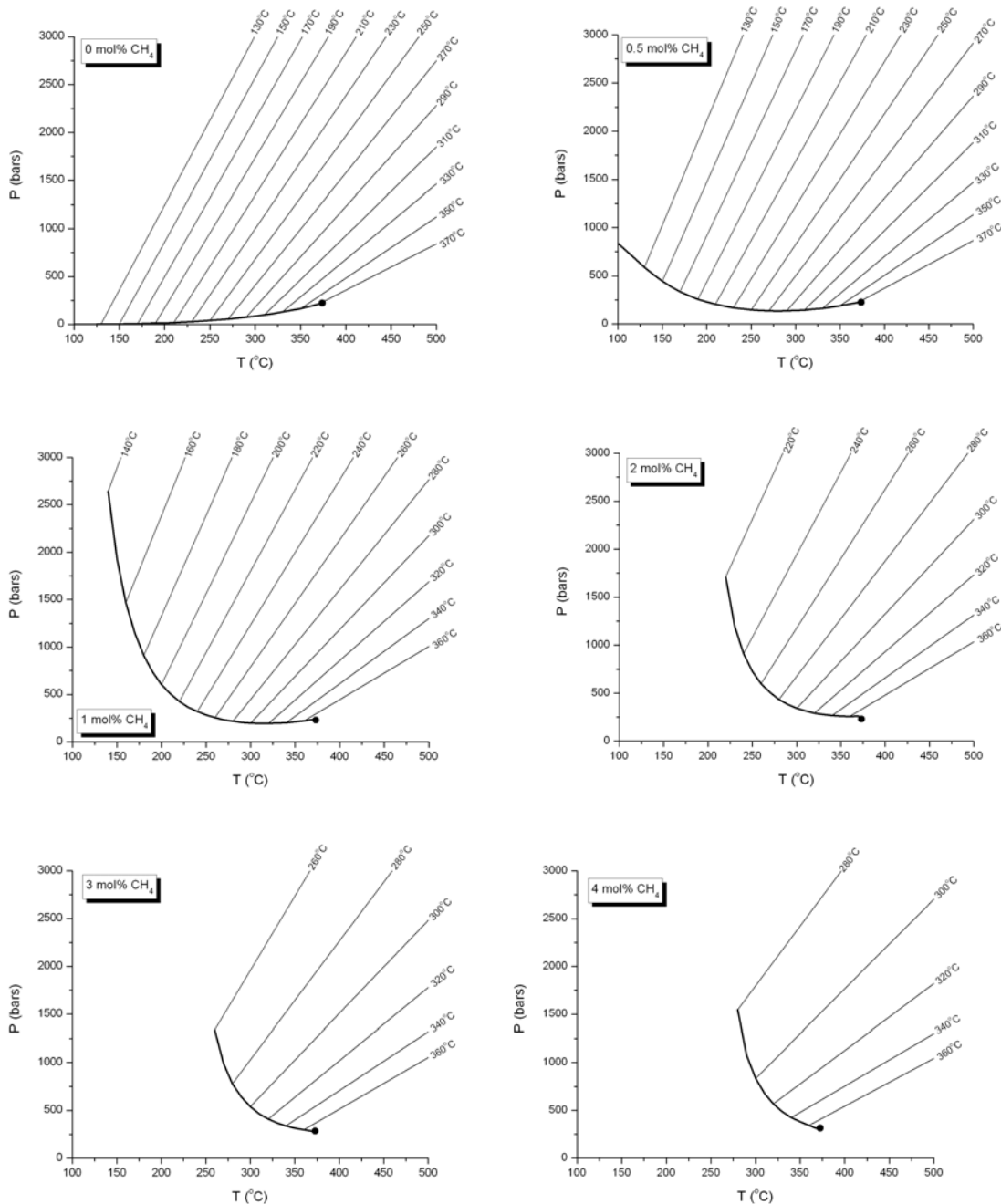


Figure 9. Iso- T_h lines for 0, 0.5, 1, 2, 3 and 4 mol% H₂O-CH₄ fluids based on the experimental results from this study. The bold lines are liquid-vapor boundaries and the black dots at the high temperature end of the liquid-vapor curves represent the critical point for that fluid composition. The iso- T_h lines are labeled with the appropriate homogenization temperature.

Chapter 3

Determination of the P-T stability limits for methane hydrate using a combined synthetic fluid inclusion and Raman spectroscopic technique

Fang Lin and Robert J. Bodnar
Department of Geosciences, Virginia Polytechnic Institute and State University,
Blacksburg, VA 24061, USA

Abstract: During recent years there has been considerable interest in the geologic occurrences and physicochemical properties of methane hydrate. This interest has been driven by the fact that methane hydrates in the seafloor and in permafrost regions of the earth represent a significant unconventional energy resource that exceeds the other fossil fuels in size. Additionally, catastrophic breakdown of methane hydrates in the geologic past may have contributed to rapid and short-lived climatic fluctuations, and may be contributing to global warming today. In order to better understand the geologic environments in which methane hydrates might be stable today or in the past, and to develop technologies for utilizing modern deposits as an energy resource, information concerning the range of P-T conditions over which methane hydrate is stable is required. Here we describe a technique that uses synthetic fluid inclusions in quartz as miniature autoclaves to study methane hydrate stability. These inclusions were analyzed by Raman spectroscopy to determine the pressure in the inclusion at the temperature of hydrate breakdown. These data define the upper temperature stability limits for methane hydrate in the system H₂O-CH₄.

1. INTRODUCTION

Methane hydrate is a naturally-occurring ice-like compound in which cages formed by water molecules contain molecules of CH₄. Methane hydrate, or clathrate, is stable at generally low temperatures and high pressures (Sloan, 1998a,b). During the past few decades interest in the occurrence and properties of natural gas (methane) hydrates has increased owing to its potential as an energy source (Kvenvolden, 1993), its potential effects on current and past climates (Hansen et al., 2000; Katz et al., 1999; Kennett et al., 2000), as an agent of submarine erosion and as a hazard to ocean-going ships (Kvenvolden, 1993, 1998, 2000). Although methane hydrates have been known since the end of the 19th century, and were recognized as an engineering obstacle in the 1930s when natural gas pipelines were built in cold climates (Deaton and Frost, 1937), little basic research into the properties and occurrence of hydrates was undertaken until fairly recently. Then, in the 1960s, a Russian drilling expedition encountered “frozen” natural gas during exploration of the Messoyakha (Myasoyakh) gas field in Siberia (Makogon et al., 1972; Kuznetsov, 2000). This led to studies to determine other environments on earth where methane hydrates might occur, and to assessment of the potential of methane hydrate as an energy resource. In the 1970s, methane hydrates were also found in submarine environments along continental margins, and in 1981 the Glomar Challenger unexpectedly encountered methane hydrate while drilling offshore Guatemala.

According to Kvenvolden and Lorenson (2001), the amount of methane carbon contained in the world’s gas hydrates in permafrost and continental margin areas is about 10,000 gigatons. This represents an amount of methane carbon that is twice as large as that contained in known deposits of coal, oil and natural gas combined! In the United States,

the gas resource within methane hydrate deposits is estimated to be 200,000 trillion cubic feet (tcf), compared to an estimated 1,400 tcf in conventional natural gas resources (USDOE, 2000). Thus, if only one percent of the methane in hydrates could be recovered, the domestic natural gas resource base would be doubled.

In addition to the interest in methane hydrates as an energy resource, it has recently been recognized that methane release from the seafloor represents a major component of the global carbon budget and that methane is an important greenhouse gas. Recently, Hansen et al. (2000) suggested that non-CO₂ greenhouse gases (including CFCs) are the main causes of global warming, with CH₄ causing the largest net climate forcing. Kennett et al. (2000) similarly proposed that rapid climatic warmings that occurred during the late Quaternary (last 800 k.y.) are the result of episodic and massive decomposition of methane hydrates on the continental margins, releasing large amounts of methane into the atmosphere. Katz et al. (1999) likewise attribute the large carbon input into the global cycle approximately 55.5 million years ago to submarine gas hydrate dissociation. Finally, Alan Judd of Sunderland University in the UK has attributed some unexplained sinkings of ships to methane hydrate dissociation (Marchant, 2000). Judd suggests that when methane hydrates on the seafloor decompose to methane gas plus water, the gas rises through the water column and lowers the density of the water and thus its buoyancy. Any ships that happen to be in this part of the ocean will “sink like a rock”. The recent discovery of a ship sitting upright on the ocean floor in an area known as the Witch Ground in the North Sea supports this hypothesis. The ship occurs in a location known as Witch’s Hole, which is a large hole or pockmark on the seafloor

thought to have been produced by the release of methane gas from dissociating hydrates in the sub-seafloor.

The potential of methane hydrate as a future energy resource, combined with its inferred effects on current and past climates has led to many studies to determine the stability limits for methane hydrates in natural geologic environments (Deaton and Frost, 1946; MeLeod and Campbell, 1961; Marshall et al., 1964; Jhaveri et al., 1965; Verma, 1974; de Roo et al., 1983; Adisasmito et al., 1991; Diamond 1994; Dickens and Quinby-Hunt, 1994; Stern, et al., 1996; Yang et al. 2001). This research complements that which has been conducted to understand the behavior of methane hydrate in oil and natural gas production and transportation environments. Here we describe a method that combines microthermometric analysis of synthetic fluid inclusions and Raman spectroscopy to determine the methane hydrate stability limits along the liquid-vapor-clathrate and ice-vapor-clathrate boundaries. The results agree with previously published experimental studies and thus provide a simple, non-destructive method to study methane as well as other gas hydrate phase equilibria *in situ*.

2. EXPERIMENTAL AND ANALYTICAL METHODS

The technique described here to determine the P-T stability limits of methane hydrate involves the formation of H₂O-CH₄ synthetic fluid inclusions with known composition, determination of the temperature of methane hydrate dissociation in the inclusions using conventional fluid inclusion microthermometric techniques, and, finally, determination of the pressure in the fluid inclusion at the temperature of methane hydrate dissociation using Raman spectroscopy.

2.1 Formation of synthetic fluid inclusions

Synthetic fluid inclusions containing known concentrations of CH₄ were prepared using techniques developed by Sterner and Bodnar (1984) and Bodnar and Sterner (1987). Quartz cores, approximately 4 mm in diameter and 5-10 mm long, and quartz prisms, about 2mm x 3mm x 5mm were cut from inclusion-free Brazilian quartz. The quartz cores and prisms were fractured by heating to 350°C, followed by immersion in cold, distilled water. After fracturing, the quartz was dried in a vacuum oven at approximately 110°C overnight.

A fractured quartz core, 20-30mg fused silica glass powder, and known amounts of aluminum carbide and distilled, deionized water were loaded into a platinum capsule (~5 mm i.d. and 25-35 mm long). Aluminum carbide (Al₄C₃) served as the source of CH₄, based upon the following reaction:



The amounts of Al₄C₃ and H₂O that were added into the Pt capsule were calculated using the above reaction stoichiometry according to the desired final CH₄ concentration. Methane gas and the aluminum hydroxide phase generated by the reaction under hydrothermal conditions were verified by Raman spectroscopy and X-ray powder diffraction analyses, respectively (Lin and Bodnar, 2004). The loaded capsules were sealed with an arc welder.

Sealed Pt capsules containing various CH₄ concentrations were loaded into horizontally-mounted cold-seal hydrothermal vessels to heal the fractures and trap synthetic fluid inclusions. The synthetic fluid inclusions produced were part of a larger experimental study to determine the PVTX properties of H₂O-CH₄ over the range of crustal PTX conditions. As such, the inclusions were formed at 300° - 700°C and 1-6 kbar. In this study, only inclusions trapped at 400° and 500°C are used because inclusions trapped at higher temperatures showed detectable amounts of CO₂. Experimental pressure was monitored using a Bourdon-type Heise gauge and is considered to be accurate to within 50-100 bars. Temperatures, measured using chromel-alumel thermocouples, are accurate to ±3°C. The capsules were quenched at the end of the run by removing the vessel from the furnace and allowing it to cool to room temperature. The capsules were cleaned to remove any residue from the surface, dried and weighed. Capsules with equal weights before and after the runs were assumed to have not leaked and were used for further analysis.

An additional check of the fluid composition inside the capsule was also conducted using the weight-loss technique described by Schmidt and Bodnar (2000). However, as it is not necessary to know the CH₄ concentration of the synthetic inclusions to determine methane hydrate P-T stability limits, the technique is not discussed in this paper. After the quartz cores/prisms were removed from Pt capsules, they were cut into thin slices and polished on both sides in preparation for microthermometric and Raman analysis. A summary of the formation conditions and analytical results is listed in Table 1.

2.2 Microthermometric analysis of synthetic fluid inclusions

The first step in determining the P-T conditions of methane hydrate stability is to determine the temperature at which the hydrate nucleates (during cooling) or dissociates (during heating). With fluid inclusions, the nucleation temperature is usually meaningless, as the inclusions must be cooled well below the equilibrium temperature to nucleate phases owing to the small sizes of the inclusions (Roedder, 1967; 1971; 1984). Therefore, the methane hydrate stability limit was determined from the temperature at which the last hydrate crystal melting upon heating from low temperature.

The melting temperature of methane hydrate in synthetic fluid inclusions was determined using a FLUID INC-adapted USGS gas-flow heating and cooling stage mounted on a Leitz Orthoplan microscope with a 40x objective with cover-glass correction. Temperature was measured using an Fe-constantan thermocouple that was calibrated using pure water (0.0°C; 374.1°C) and H₂O-CO₂ synthetic fluid inclusions (Sternner and Bodnar, 1984). The accuracy over the range of interest here (approximately -40° to +40°C) is ±0.1°C. It should be noted that the FLUID INC-adapted USGS gas-flow heating and cooling stage was used to determine the hydrate melting temperatures, but that a Linkam stage was used for inclusion analyses on the Raman microprobe. The gas-flow stage provides better temperature control when doing thermal cycling to accurately determine temperatures of phase changes, but it cannot be used effectively to maintain a constant temperature as is required during Raman analyses. Additionally, the gas-flow stage design places three glass windows between the sample and the microscope objective, significantly increasing the working distance and decreasing the Raman signal intensity at the detector. Thus, the two different stages were used to make best use of the advantages of each stage for this project.

A thermal cycling technique was used to determine the hydrate dissociation temperature in the inclusions (Goldstein and Reynolds, 1994). At room temperature the inclusions contain a CH₄-saturated aqueous phase and a vapor bubble that is essentially pure CH₄ (Fig. 1A). The sample was cooled to -180°C at 50°C/min. Metastable liquid water remains in the inclusions until about -30°C, at which point methane hydrate and ice instantaneously nucleate (Fig. 1B) and the pressure in the inclusion decreases to that along the Hydrate+Ice+Vapor line (H-V-I; Fig 1). As the inclusion is heated it follows the Hydrate+Ice+Vapor line to the quadruple point (Q; Fig. 1) at approximately -0.2°C, where liquid water forms as the ice phase melts. At this temperature, methane hydrate + CH₄-rich vapor phase + ice + CH₄-saturated aqueous phase (L_w) are in equilibrium. When heated beyond the invariant point, the ice phase disappears resulting in an inclusion containing methane hydrate + CH₄-rich vapor phase + CH₄-saturated aqueous phase (Fig. 1D). With continued heating the inclusion follows this three-phase equilibrium curve (H-V-L_w; Fig. 1) and hydrate continuously dissociates to aqueous solution + CH₄-rich vapor, increasing the pressure in the inclusion. The vapor bubble becomes more rounded (Fig. 1E) as hydrate dissociates and no longer interferes with and distorts the vapor phase.

The exact temperature at which hydrate completely disappears is difficult to determine optically owing to the small size of the inclusions. To determine whether the hydrate had completely disappeared, the sample is cooled by several degrees Celsius. If hydrate remains in the inclusion to serve as a nucleus, the vapor bubble will become noticeably smaller during cooling as CH₄ is removed from the vapor and incorporated into hydrate. In this case, hydrate will grow and the vapor bubble will again become distorted owing to interference with the solid hydrate (Fig. 1F, G and H). If the hydrate

had completely disappeared, the inclusion would remain unchanged during cooling and would not change appearance until nucleation of ice and hydrate occurred after several tens of degrees of supercooling below the equilibrium temperature, as observed during the initial cooling cycle.

If hydrate remains, the inclusion is then heated to a temperature 0.1°C above the previous maximum temperature, cooled, and the behavior of the bubble observed. This process is repeated until no change is observed in the inclusion during cooling, signaling that the hydrate phase had completely melted.

It should be noted that hydrate dissociation is very sluggish. Therefore, a slow heating rate (less than 15°C/minute) is required to produce “equilibrium clathrate” crystals (Murphy and Roberts, 1997). If a fast heating and cooling rate is used, metastability occurs as evidenced by a sudden burst of hydrate clusters upon cooling, rather than gradual growth of hydrate crystals at the hydrate-aqueous phase interface.

2.3 Raman analysis

Raman spectroscopy was used to confirm the presence or absence of methane hydrate and other phases/components in the synthetic fluid inclusions, to determine the methane symmetric stretching band position at the temperature of final hydrate melting, and to develop the calibration equation describing the relationship between the methane peak position and temperature and pressure.

Raman analyses were conducted in the Vibrational Spectroscopy Laboratory in the Department of Geosciences at Virginia Tech. Analyses were conducted on JY Horiba LabRam HR (800mm) spectrometer, with 1800 grooves/mm gratings and using a slit

width of 150 μm , resulting in a theoretical spectral resolution of the detector of $\pm 1.37 \text{ cm}^{-1}$ (Paroli and Butler, 1990). Excitation was provided by a 514.57 nm Laser Physics 100S-514 Ar^+ laser. The laser output was 50mW at the source and 2-3 mW at the surface of a sample after passing through a 40x objective. The detector is an electronically-cooled open electrode CCD. Raman spectra were collected using a 3.5x objective with the pressure cell (described below) or a 40x objective with cover glass correction (Adar et al., 2004) for fluid inclusions in the heating/cooling stage. Five accumulations of 1 sec were used for pressure cell measurements, and 2 accumulations of 60 sec were used for fluid inclusions.

Calibration of the position of the methane symmetric stretching band position as a function of pressure and temperature was accomplished using a high-pressure optical cell. The cell was constructed from a standard three-way, two-stem, 15,000 psi combination valve (High Pressure equipment, Model #10-15AF6) made from 316 stainless steel (Fig. 2). A 1/2 inch, threaded hole was drilled into the center of the cell and halfway through the thickness. A smaller hole was then drilled from the bottom of this hole to a distance of 16 mm from the bottom of the valve body. An O-ring and round, 3.2 mm thick silica glass window was inserted into the hole and held in place with a stainless steel retainer ring. The cell was connected to a manual pressure generator (High Pressure equipment Model #50-6-15) and pressure was monitored using a Precise Instruments pressure transducer (Model 645) accurate to $\pm 0.10\%$ of the pressure output. Ultra-high purity methane was used for the calibration and the system was purged several times before each experiment to remove any other gases and/or water from the system. Raman peak positions were measured in 2 bar increments in the 1-250 bar range and in 5 bar

increments in the 250-600 bar range at 22°C (room temperature). For all other temperatures, the maximum calibrated pressure was 300 bars, and the peak position was measured in 5 bar increments at 1°C and in 50 bar increments at all other temperatures (0.3, 2, 4, 6, 8, 10, 12, 14, 16, 18 and 20°C). The Raman peak positions were recorded both during increasing and decreasing pressure cycles. The mean value of the two measurements was taken as the Raman peak position at that pressure, although the difference between the two measurements was generally less than $\pm 0.03 \text{ cm}^{-1}$.

The pressure cell was immersed in a water bath to control the temperature. An Omega type-E thermocouple, calibrated against water freezing point at 0°C, was inserted into a small hole drilled at the top of the pressure cell, 10 mm deep and 5 mm away from the gas chamber, to monitor the temperature.

Due to the nonlinear behavior of the monochromator, the spectrometer position was calibrated in the spectral region of interest to optimize accuracy in the peak position measurement. Two emission lines from a neon calibration lamp that was permanently fixed within the optical path of the microscope were recorded together with each CH₄ Raman scattering emission. Figure 3 shows an example of simultaneously collected CH₄ and Ne spectra. The 2851.50 and 2972.57 cm^{-1} Ne lines were used for calibration. These lines closely bracket the position of the methane peak (occurring at 2913.26 cm^{-1} on Fig. 3). According to McCreery (2000), the actual positions of the two Ne lines are 2851.38 and 2972.44 cm^{-1} , respectively, relative to a 514.5nm excitation laser. Using the measured peak positions for the CH₄ symmetric stretching band and the measured and real peak positions for the Ne 2851.38 and 2972.44 cm^{-1} lines, the corrected (real)

position for the methane peak (2913.14 cm⁻¹ for the example in Fig. 3) is given by the following expression:

$$v_{corr}^{CH_4} = \frac{1}{2} \{ [v_{meas.}^{CH_4} + (v_{real}^{Ne,2851.38} - v_{meas.}^{Ne,2851.38})] + [v_{meas.}^{CH_4} + (v_{real}^{Ne,2972.44} - v_{meas.}^{Ne,2972.44})] \}$$

The peak position of each measured Raman scattering line was determined using Gauss/Lorentz peak fitting after baseline correction.

Recording the two Ne emission lines during each analysis is necessary for accurate quantification. We found that the Ne emission lines systematically shift to higher frequency with time after the initial calibration. This can significantly affect the calculation of the position of the CH₄ peak and, therefore, the determination of CH₄ pressure. Fortunately, the relative positions of the two Ne lines are essentially constant at 121.06±0.03 cm⁻¹.

As noted above, fluid inclusions were analyzed using a Linkam THMSG600 heating/cooling stage mounted on an Olympus BX41 microscope attached to the Raman microprobe, using a 40x coverslip-corrected objective (Adar et al., 2004). The Linkam stage offered better temperature stability and higher Raman signal throughput, compared to the FLUID INC-adapted gas-flow stage used to determine the temperature of hydrate melting. The Linkam stage was also calibrated using pure water (0.0°C; 374.1°C) and H₂O-CO₂ (-56.6°C) and the accuracy over the range of interest here (-40°C to +40°C) is ±0.1°C.

The Raman microprobe was used to determine the position of the methane symmetric stretching band in the inclusion (for pressure determination) and to confirm the presence or absence of hydrate in the inclusions (Fig. 4). The Raman peak doublet in

the range 2903-2915 cm^{-1} is diagnostic for methane hydrate and is distinct from the single peak for methane gas that occurs near 2917 cm^{-1} (Sum et al. 1997).

3. RESULTS AND DISCUSSION

3.1 Effect of temperature and pressure on the CH_4 peak position

The Raman peak position for CH_4 gas is known to shift systematically from $\sim 2917 \text{ cm}^{-1}$ at 1 atm to lower wavenumber as pressure increases (Herzberg, 1968; Fabre and Couty, 1986; Seitz et al., 1993; Thieu et al., 2000). However, there is disagreement between the results of various studies (Fig. 5). Moreover, any correlation between peak position and temperature *and* pressure had not been examined previously.

The position of a Raman band reflects the frequency of a specific vibration mode of the molecule. The Raman spectrum uniquely identifies a molecular species, making this technique useful in the qualitative analysis of complex mixtures. However, the exact vibration frequency (peak position) changes as a function of the molecular environment. Previous workers (May et al, 1959; Fabre and Couty, 1986; Seitz, 1996; Thieu et al., 2000) showed that the CH_4 symmetric stretching band shifts to lower relative wave number as density increases. Figure 5 summarizes the work by Thieu et al. (2000) and Fabre and Couty (1986) as well as results from this study. While all three studies show that the peak position systematically shifts to lower wavenumber as pressure increase, significant difference does exist between the different data sets.

The discrepancy between the different data sets shown on Figure 4 may be due to different calibration methods and spectrometer settings used by the different investigators. Thieu et al (2000) used three Ne emission lines for calibration, but the assumed positions

of two lines used in their calibration (2852.6 and 2973.3 cm^{-1}) were at higher frequency compared to ours (2851.38 and 2972.44 cm^{-1}). However, making a correction for the different assumed values for the neon lines still does not bring the two datasets into coincidence. Fabre and Couty (1986) used only one spectral line from an argon lamp for calibration. It is generally assumed that using two lines that bracket the position of the unknown line results in better calibration. The three datasets shown on Figure 5 were also collected at different temperatures. Measurements of Thieu et al (2000) were conducted at 298 K, ours were at 295K and those of Fabre and Couty were at 293K. We note, however, that temperature differences alone cannot account for the discrepancies between the three datasets, as described in detail below. We also note that calibrations done on two similar (both JY Horbia LabRam HR) but separate Raman microprobes in the authors' laboratory resulted in two different calibration results. Therefore, it appears that the pressure – Raman peak position correlation is instrument-specific, as has been shown previously by Pasteris et al. (1988). The good news is that the calibration is reproducible on the same spectrometer.

To investigate the effect of temperature on CH_4 Raman peak position, the symmetric stretching band position was determined in the 0.3-22°C and 1-300 bars using the optical cell described earlier (Fig. 6, called “v-P” diagram hereafter). Analyses were conducted along 13 isotherms. At any pressure in the studied P-T range, the CH_4 peak shifts to lower wavenumber as temperature decreases. The temperature dependence of the Raman peak shift is smaller at lower pressures, reaches a maximum at about 200 bars, and decreases slightly at higher pressures. Step-wise multiple regression analysis of the

362 datasets from our experiments shows that the data can fit into the following equation with an R^2 value of 0.9994:

$$\nu_{1,CH_4} = 2917.55852 - \sum_{i=0}^4 \sum_{j=0}^4 a_{i,j} \cdot P^i \cdot T^j \quad (2)$$

The fitting parameters in equation (2) are listed in Table 2.

The effect of temperature and pressure on the CH_4 Raman peak position correlates with the manner in which the CH_4 density varies over this same P-T range (Friend et al., 1989). Figure 7 shows the change in density (Δd) in going from 295K, 1 bar, to various P-T conditions in the range 270 – 295K and 5-200 bars, plotted against the relative change in measured Raman shift compared to the peak position at 295K and 1 bar ($\Delta \nu$). The good correlation between the CH_4 Raman peak shift and the density change of CH_4 suggests that the shift in Raman peak position represents a fundamental change in the nature of bonding in the methane molecule as density changes and interactions between molecules change (Lin et al., in prep).

3.2 Determination of methane hydrate stability limits

The temperature at which the hydrate phase melted was determined by thermal cycling in the heating/cooling stage, and confirmed by Raman analysis. Once the final melting temperature of methane hydrate was determined, the Raman spectrum of the CH_4 -rich bubble in the two-phase (liquid plus vapor) H_2O - CH_4 inclusion was collected at that temperature. The peak position of CH_4 symmetric stretch band at that temperature was calculated, and the pressure inside the CH_4 -rich bubble at that temperature was determined based on the relationship between methane pressure and the temperature and

peak position (Fig. 6). Seventeen inclusions, representing 17 different P-T formation conditions and methane concentrations, were analyzed and the results are shown in Figure 8. Also shown for comparison are hydrate stability limits calculated using the thermodynamics-based CSMHYD model (Sloan, 1998a) and the computer model of Bakker which is based on the Duan et al (1992) equation of state (Bakker and Brown, 2002, abbreviated as “Bakker model” hereafter), along with previously published experimental data. In all of the inclusions used in this study, hydrate melting temperatures are higher than the ice melting temperatures. Therefore, the determination of hydrate stability is limited to the H-V-L_w three-phase equilibrium line. Methane hydrate stability limits determined from synthetic fluid inclusions are in general agreement with the results from both the theoretical models and experimental studies. In the higher P-T range ($T > \sim 15^{\circ}\text{C}$, $P > \sim 120$ bars), experimental data from this study and from the previous studies show a slightly elevated pressure, or a slightly depressed temperature, compared to the CSMHYD results. However, the experimental data appear to agree well with results from the Bakker model over the entire range.

3.3 Hydrate stability limits from analyses of single inclusions

The results presented above for methane hydrate stability are based on a single data point obtained from each inclusion. That is, the temperature and pressure at which the final hydrate melting occurred was determined and this represented one P-T point on the methane hydrate stability curve. However, a great advantage of the synthetic fluid inclusion technique (or any optical cell technique) is that many data points can be acquired from a single loading (or single composition). As noted previously, when the

fluid inclusions are cooled and ice and hydrate nucleate, the inclusion pressure drops to the hydrate+ice+vapor equilibrium line in P-T space (H-V-I; Fig 1). Thus the temperature and pressure inside the inclusion represent the temperature and pressure on the equilibrium line. Similarly, the location of the quadruple point (Q, Fig. 1) can be determined by determining the temperature and pressure at which the inclusions contains the four phases hydrate+ice+vapor+liquid, and the hydrate+vapor+liquid equilibrium (H-V-L_w; Fig. 1) can be determined for any P-T condition at which the inclusion contains those three phases.

Four synthetic H₂O-CH₄ inclusions with different bulk compositions and densities were analyzed. The synthetic inclusions were trapped at 400-500°C, 2-6 kbars and contained 1.7-14.0 mol% CH₄. Each inclusion was cooled to nucleate the assemblage hydrate+ice+vapor, and then heated incrementally and analyzed by Raman at each temperature increment. Only two of the four compositions contained inclusions that were large enough and with sufficient CH₄ for analysis along the H-I-V line. The inclusions were analyzed every 1°C along the H-V-L_w line and every 5-10°C along the H-V-I three-phase equilibrium line. The inclusions were held at temperature for at least 2 minutes before the Raman spectrum was collected (analyses after allowing the inclusions to equilibrate for longer times, i.e., 4-5 minutes, did not show noticeable difference). The results are plotted on Fig. 9, together with phase relations predicted from the CSMHYD model and the Bakker model, as well as experimental data from previous studies.

Methane hydrate stability limits determined from Raman analysis of synthetic fluid inclusions show excellent agreement with previously published results. However, as found previously, all the experimental data, including ours, suggest that the H-V-L_w

three-phase line is slightly depressed in temperature (or elevated in pressure) in the higher temperature and higher pressure range, compared to phase relations predicted by the CSMHYD model. The experimental data show better agreement with the results predicted by the Bakker model. For temperatures lower than 0.3°C or higher than 22°C (i.e. outside the range of the calibration data), pressures were estimated assuming that the peak position-temperature correlation is linear and was extrapolated to either lower or higher temperatures. This assumption appears to be valid, as methane hydrate phase relations determined for temperatures below 0°C agree well with those from the two theoretical models. In fact, the technique described here appears to be valid for determining methane hydrate phase equilibria along the H-V-I line, which can not be accomplished easily using conventional aqueous chemistry methods (Sloan, 1998a).

After the hydrate completely dissociates, with further heating the inclusion follows a path (essentially an isochore) through the $L_w+V_{CH_4}$ two-phase field. Within this region the pressure in the inclusion increases more gradually with increasing temperature (compared to the H-V- L_w phase boundary), and is controlled by the vapor pressure of the gas phase. The increase in pressure with increasing temperature in the $L_w+V_{CH_4}$ region is essentially linear over small temperature intervals (Fig. 9). As a result, the final melting temperature of methane hydrate can also be predicted based on the temperature at which this “break in slope” of the P vs. T occurs. In fact, we found that hydrate final melting temperatures determined by this means are identical ($\pm 0.5^\circ\text{C}$) to those determined using the thermal cycling technique.

The outstanding feature of the single inclusion technique is that by using an appropriate inclusion, combined with microthermometry and Raman spectroscopy,

methane hydrate stability limits in P-T space can be determined quickly and accurately. After the instrument-specific methane peak position-temperature-pressure correlation was established, the average time needed to determine the phase relations at any P-T condition is about 5 minutes, and phase equilibria over the temperature range from -40 to $\sim 30^{\circ}\text{C}$ can be determined within a few hours. Future studies will apply this technique to other gas hydrate systems as well as saline aqueous solutions.

4. ERROR ANALYSIS

The error in temperature measurements in this study is $\pm 0.05^{\circ}\text{C}$, determined by measuring the freezing point of a pure H_2O inclusion. Although laser-induced heating of fluid inclusions is commonly a concern, there is no evidence to suggest that the temperature in a $\text{H}_2\text{O}-\text{CH}_4$ inclusion is measurably different from that recorded by the thermocouple during Raman analysis. In a previous Raman spectroscopic study of CO_2 -bearing inclusions by Rosso and Bodnar (1995), using a laser power of 300-1000 mW at the source and 60-240 seconds of acquisition time, no measurable heating was detected. In this study the laser power was only 50 mW at the source (2-3 mW at the sample surface, using a 40x objective) and the acquisition time was also shorter (2 accumulations of 60 sec). Also, we were able to focus the laser on a CO_2 inclusion that contains both liquid and vapor carbon dioxide, and the CO_2 phases do not homogenize. This means that the inclusions were not heated to greater than 31°C (the critical temperature of carbon dioxide) by the laser. Carbon dioxide is a stronger absorber of thermal energy than methane, so any heating of methane-bearing inclusions should be even less than for carbon dioxide.

The error involved in determination of pressure inside an H₂O-CH₄ inclusion is complicated and involves several parameters.

(1) The error in the methane peak position ($\sigma_{v,tot}$) determined during calibration has two sub-components. This first is the error in the measured methane peak position during calibration. The methane peak positions used here are mean values of the peak positions based on several measurements. We calculated the standard deviation (σ) of the methane peak position at each pressure, and there does not appear to be any correlation with pressure. In order to determine the error at all pressure conditions and to reduce the random effect of experiments, the average standard deviation (σ_{ave}) was also calculated. For the 160 data sets that we have measured, σ_{ave} is about 0.0146cm^{-1} . The second component of error in the methane peak position comes from the error in the simulated peak position (σ_{sim}) associated with peak-fitting. Peak positions for each analysis were determined using a Gauss-Lorentz peak-fitting function. The error due to the peak-fitting process used in the software (σ_{sim}) was small ($\pm 0.005\text{cm}^{-1}$) using the optimized fitting parameters. Therefore, the total error in the methane peak position ($\sigma_{v,tot}$) during calibration is the sum of the error associated with spectra accumulation (σ_{ave}) and the error from peak-fitting (σ_{sim}) or simulation, which approximately equals 0.02cm^{-1} . That is, the total error in the measured methane peak position is $\pm 0.02\text{cm}^{-1}$.

(2) Error propagation ($\sigma_{v,p}$) on the pressure determination. Due to the non-linear correlation between the applied pressure and the measured methane peak position shown on the ν -P diagram, $\pm 0.02\text{cm}^{-1}$ error in methane peak position would result in a larger absolute error in the pressure estimation in the higher pressure range than in the lower pressure range. This is because the ν -P curve becomes steeper at higher pressures. For

instance, at a pressure of 20 bars, $\sigma_{v,p} = \pm 1$ bars in response to $\sigma_{v,tot}$ of $\pm 0.02 \text{ cm}^{-1}$; At a pressure of 300 bars, $\sigma_{v,p} = \pm 2.5$ bars for the same peak position error range along the 22°C v–P curve. In addition, the curvature of the v–P curves is temperature-dependent. In the investigated temperature range (1– 22°C) the slope of the v–P curve increases with increasing temperature. The previous estimation of error propagation was based on the 22°C v–P curve, therefore it represents the maximum error in the studied temperature range and the errors should be smaller for the other temperature conditions.

(3) Error of the pressure (σ_p) used for calibration. The manufacturer calibrated pressure gauge used to measure the pressure inside the pressure cell has an accuracy of 0.1% of output pressure, which makes the discrepancy between the output pressure and the real pressure almost negligible in the investigated pressure range (0.02 bar at 20 bars and 0.3 bar at 300 bars). However, the maximum readability of the pressure gauge was 1 bar, which limited the precision of the measured pressure to be ± 0.5 bars over the entire pressure range.

The total error in the pressure determined by our method ($\sigma_{p,tot}$) is the sum of the error propagated from peak position determination ($\sigma_{v,p}$) and the error from pressure calibration (σ_p). At 22°C , $\sigma_{p,tot}$ is ± 1.5 bar at 20 bars and ± 3 bars at 300 bars. At the other temperatures ($<22^\circ\text{C}$), the error in pressure will be even smaller.

5. SUMMARY

This technique described here combines microthermometry and Raman spectroscopic analysis of synthetic fluid inclusions to determine methane hydrate phase equilibria in P-T space quickly and accurately. Synthetic fluid inclusions are ideal to

demonstrate hydrate formation and dissociation, and are highly portable and reusable and can be analyzed in multiple laboratories to test for uniformity. The average time needed to determine the phase relations at any P-T condition is about 5 minutes, and phase equilibria over the temperature range from -40 to $\sim 30^{\circ}\text{C}$ can be determined within a few hours. Error analysis indicates that pressure determinations are accurate to ± 1.5 bars at 20 bars and ± 3 bars at 300 bars and 22°C . The error in pressure decreases with decreasing temperature. This technique can be applied to study phase equilibria in other gas hydrate systems, including those involving saline aqueous solutions, and can be used to investigate the kinetics of hydrate reactions, which are difficult to study using more conventional techniques.

Acknowledgements—The authors wish to thank Mr. Charles Farley for his enormous help on experimental setup and thank Dr. Jing Zhao for discussions on Raman spectroscopy and data processing. Comments on an earlier version of this manuscript by Drs. P. Dove, F. Read, M. Schreiber and A. Sum are greatly appreciated.

References

- Adar F., Naudin C., Whitley A. & Bodnar R. J. (2004) Use of a microscope objective corrected for a cover glass to improve confocal spatial resolution inside a sample with finite index of refraction. *Appl. Spectrosc.* **58**, 1136-1137.
- Adisasmito S., Frank R. J. III and Sloan E. D, Jr. (1991) Hydrates of carbon dioxide and methane mixtures. *J. Chem. Eng. Data* 36, 68-71.
- Bakker R. and Brown P. (2002) Computer modelling in fluid inclusion research. In *Fluid Inclusions: Analysis and Interpretation* (eds. I. Samson, A. Anderson and D. Marshall), Mineralogical Association of Canada, Short-course Volume 32.
- Bodnar R. J. and Sterner S. M. (1987) Synthetic Fluid inclusions. In *Hydrothermal Experimental Techniques* (eds. G. C. Ulmer and H. L. Barnes), Chap.17. John Wiley and Sons. pp. 432-457.
- Deaton W. M. and Frost E. M. (1937) Gas hydrates in natural gas pipe lines. *Oil & Gas Journal* 36, 75
- Deaton W. M. and Frost E. M. Jr. (1946) Gas Hydrates and Their relation to the operation of Natural-Gas Pipe Lines, U.S. Bureau of Mines Mono., No.8. pp.101.
- Diamond L. W. (1994) Salinity of multivolatile fluid inclusions determined from clathrates hydrate stability. *Geochim. et. Cosmochim. Acta* 58, 19-41.
- Dickens G. R. and Quinby-Hunt M. S. (1994) Methane hydrate stability in seawater. *Geophysical Research Letters* 21, 2115-2118.
- Duan Z., Møller N. and Weare J. H. (1992) An equation of state for the CH₄-CO₂-H₂O system: II. Mixtures from 50 to 1000°C and 0 to 1000 bar. *Geochim. et. Cosmochim. Acta* 56, 2619-2631.
- Fabre D. and Couty R. (1986) Etude par spectroscopie Raman du méthane comprimé jusqu'à 3 kbar: Application à la mesure de pression dans les inclusions fluides contenues dans les minéraux. *Comptes Rendu Acad. Sc. Paris*, 303, Série II, no. 14, 1305-1308 (in French).
- Friend D. G., Ely J. F. and Ingham H. (1989) Tables for the thermophysical properties of Methane. NIST Technical Note 1325, U.S. Department of Commerce/National Institute of Standards and Technology.
- Goldstein R. H and Reynolds T. J. (1994) Systematics of fluid inclusions in diagenetic minerals. *SEPM Short Course*, volume 31, 199pp.

Hansen J., Sato M., Ruedy R., Lacis A. and Oinas V. (2000) Global warming in the twenty-first century: An alternative scenario. *Proceedings of the National Academy of Science*, 97, 9875-9880.

Herzberg G. (1968) *Molecular spectra and molecular structure: II. Infrared and Raman spectra*. Van Nostrand, London, 632 pp.

Jhaveri J. and Robinson D. B. (1965) Hydrates in the Methane-nitrogen System. *Can. J. Chem. Eng.* 43, 75.

Katz M. E., Pak D. K., Dickens G. R. and Miller K. G. (1999) The source and fate of massive carbon input during the latest Paleocene thermal maximum. *Science* 286, 1531-1533.

Kennett J. P., Cannariato K. G., Hendy I. L. and Behl R. J. (2000) Carbon isotopic evidence for methane hydrate instability during Quaternary interstadials. *Science* 288, 128-133.

Kuznetsov F. A. (2000) Gas hydrates of Siberia. In. *Gas Hydrates: Challenges for the Future*, Holder, G.R. and Bishnoi, P.R., (eds.), *Annals of the New York Academy of Science*, 912, 101-111.

Kvenvolden K. A. (1993) Gas hydrates (clathrates) in the geosciences; resource, hazard, and global change. *AAPG Bulletin* 77, 2020.

Kvenvolden K. A. (1998) A primer on the geologic occurrence of gas hydrate. In. Henreit, J.-P. & Mienert J. (eds.) *Gas Hydrates: Relevance to World Margin Stability and Climate Change*. Geological Society of London, Special Publication 137, 9-30.

Kvenvolden K. A. (2000) Gas hydrate and humans. In. *Gas Hydrates: Challenges for the Future*, Holder, G.R. and Bishnoi, P.R., (eds.), *Annals of the New York Academy of Science* 912, 17-22.

Kvenvolden K. A. and Lorenson T. D. (2001) Global occurrence of gas hydrate. The proceedings of the Eleventh (2001) international offshore and polar engineering conference 11, 462-467.

Lin, F. and Bodnar, R.J. (2004) Experimental Study of the PVTX Properties of Water-Methane, *EOS Transaction, AGU*, 85(47), Fall Meeting Supplement, Abstract T41B-1206.

Lin F., Sum A. and R. J. Bodnar (2006) Pressure and temperature sensitivity of methane Raman line shift at near room temperatures: Understanding the shift at the molecular level. (in preparation).

- Makogon Y. F., Trebin F. A., Trofimuk A. A., Tsarev V. P. and Cherskiy N. V. (1972) Detection of a pool of natural gas in a solid (hydrate gas) state. Doklady Academy of Sciences U.S.S.R., Earth Science Section, 196, 197-200.
- Marchant J. (2000) Monsters of the deep. New Scientist, no. 2267, December 2, 2000, 20-21.
- Marshall D. R., Saito S. and Kobayas R. (1964) Hydrates at high Pressures: Part I. Methane-Water, Argon-Water, and Nitrogen-Water Systems, A. I. Ch. E. Journal 10, 202-205.
- May A. D., Stryland J. C. and Welsh H. L. (1959) Raman spectra of H₂ and CH₄ at high pressure. Journal of Chemical Physics 30, 1099-1100.
- McCreery R. L. (2000) Raman spectroscopy for chemical analysis. John Wiley & Sons, New York. 420p.
- McLeod H. O. Jr. and Campbell J. M. (1961) Natural gas hydrates at pressure to 10,000 psia. Journal of Petroleum Technology 12, 590-594.
- Murphy P. J. and Roberts S. (1997) Melting and nucleation behaviour of clathrates in multivolatile fluid inclusions: evidence of thermodynamic disequilibrium. Chemical Geology 135, 1-20.
- Paroli R. M. and Butler I. S. (1990) A handy indicator of resolution in Raman spectroscopy. Applied Spectroscopy 44, 1414-1415.
- Pasteris J. D., Wopenka B. and Seitz J. C. (1988) Practical aspects of quantitative laser Raman microprobe spectroscopy for study of fluid inclusions. Geochimica et Cosmochimica Acta 52, 979-988.
- Roedder E. (1967) Metastable superheated ice in liquid-water inclusions under high negative pressure. Science 155, 1413-1417.
- Roedder E. (1971) Metastability in Fluid Inclusions. Soc. Mining Geol. Japan, Spec. Issue 3, 327-334.
- Roedder E. (1984) Fluid inclusions. Reviews in Mineralogy, vol.12. Mineralogical Society of America, 644pp.
- Rosso K. M. and Bodnar R. J. (1995) Microthermometric and Raman spectroscopic detection limits of CO₂ in fluid inclusions and the Raman spectroscopic characterization of CO₂. Geochimica et Cosmochimica Acta 59, 3961-3975.

- Schmidt C. & Bodnar R. J. (2000) Synthetic fluid inclusions: XVI. PVTX properties in the system H₂O-NaCl-CO₂ at elevated temperatures, pressures, and salinities. *Geochimica et Cosmochimica Acta*, 64, 3853-3869.
- Seitz J. C., Pasteris J. D. and Chou I-M. (1993) Raman spectroscopic characterization of gas mixtures. I. Quantitative composition and pressure determination of CH₄, N₂ and their mixtures. *American Journal of Science* 293, 297-321.
- Seitz J. C., Pasteris J. D. and Chou I-M. (1996) Raman spectroscopic characterization of gas mixtures. II. Quantitative composition and pressure determination of the CO₂-CH₄ system. *American Journal of Science* 296, 557-600.
- Sloan E. D., Jr. (1998a) *Clathrate hydrates of natural gases*, 2nd. Ed. Marcel Dekker, New York.
- Sloan E. D., Jr. (1998b) Gas hydrates: Review of physical/chemical properties. *Energy & Fuels* 12, 191-196.
- Stern L. A., Kirby S. H., and Durham W. B. (1996) Peculiarities of Methane Clathrate Hydrate Formation and Solid-State Deformation, Including possible Superheating of Water Ice. *Science* 273, 1843-1848.
- Sterner S. M. and Bodnar R. J. (1984) Synthetic fluid inclusions in natural quartz. I. Compositional types synthesized and applications to experimental geochemistry. *Geochimica et Cosmochimica Acta* 48, 2659-2668.
- Sum A. K., Burruss R. C. and Sloan E. D., Jr. (1997) Measurement of clathrate hydrates via Raman spectroscopy. *Journal of Physical Chemistry B* 101, 7371-7377.
- Thieu V., Subramanian S., Colgate S. O. and Sloan E. D., Jr. (2000) High-pressure optical cell for hydrate measurements using Raman spectroscopy. In: *Gas Hydrates: Challenges for the Future* (eds. G. R. Holder and P. R. Bishnoi). *Annals of the New York Academy of Science* 912, 983-992.
- Verma V. K. (1974) *Gas Hydrate from Liquid Hydrocarbon-Water Systems*. Ph.D. Thesis, University of Michigan, Ann Arbor, MI.
- Yang S. O., Cho S. H., Lee H. and Lee C. S. (2001) Measurement and prediction of phase equilibria for water + methane in hydrate forming conditions. *Fluid Phase Equilibria* 185, 53-63.

Table 1. Formation conditions of the synthetic fluid inclusions.

Inclusion I.D.	T _f (°C) ^a	P _f (kbars) ^b	X (mol%CH ₄) ^c	T _{Hdiss} (°C) ^d	v _{CH4} (cm ⁻¹) ^e	P _{Hdiss.} (bars) ^f
091504-6-21	500	1	2.77	0.5	2917.02	26
091504-7-20	500	1	3.76	2.4	2916.85	33
051304-4-3	500	1	3.45	2.7	2916.90	32
111004-4-10	500	3	1.07	3.0	2916.93	31
092604-5-x	500	2	1.67	3.7	2916.85	32
092604-6-23	500	2	2.33	5.6	2916.66	44
092604-7-x	500	2	2.87	7.3	2916.77	54
111004-2-16	500	3	2.23	8.4	2916.21	61
111004-5-x	500	3	3.09	9.7	2915.86	75
0622997-1-1	400	5	1.93	11.8	2915.57	87
0218993-3-1	400	3	2.41	12.0	2915.47	92
0218993-3-2	400	3	2.41	12.0	2915.50	90
0622997-1-2	400	5	1.93	14.6	2914.65	126
0218993-1-1	400	3	4.08	14.9	2914.59	128
0218993-1-2	400	3	4.08	15.1	2914.53	133
0622997-2-1	400	5	3.66	18.5	2913.19	213
0622997-2-2	400	5	3.66	18.5	2913.15	214

a – temperature at formation

b – pressure at formation

c – CH₄ concentration

d – temperature at hydrate final dissociation

e – CH₄ Raman peak position at hydrate final dissociation temperature

f – pressure at hydrate final dissociation

Table 2. Fitting parameters in equation (2)*.

Fitting Parameters	
$a_{0,0}$	0
$a_{1,0}$	-0.01554
$a_{2,1}$	4.08E-6
$a_{2,0}$	-1.796E-4
$a_{3,1}$	-2.51084E-8
$a_{3,0}$	9.319009E-7
$a_{4,0}$	-1.28013E-9
$a_{4,1}$	4.21377E-11
$a_{2,4}$	4.04584E-10
$a_{4,4}$	1.18729E-15
$a_{1,4}$	-3.89847E-8
$a_{0,4}$	9.55892E-7
$a_{3,4}$	-1.3072E-12

* all the fitting parameters which are not listed in the table have a value of zero.

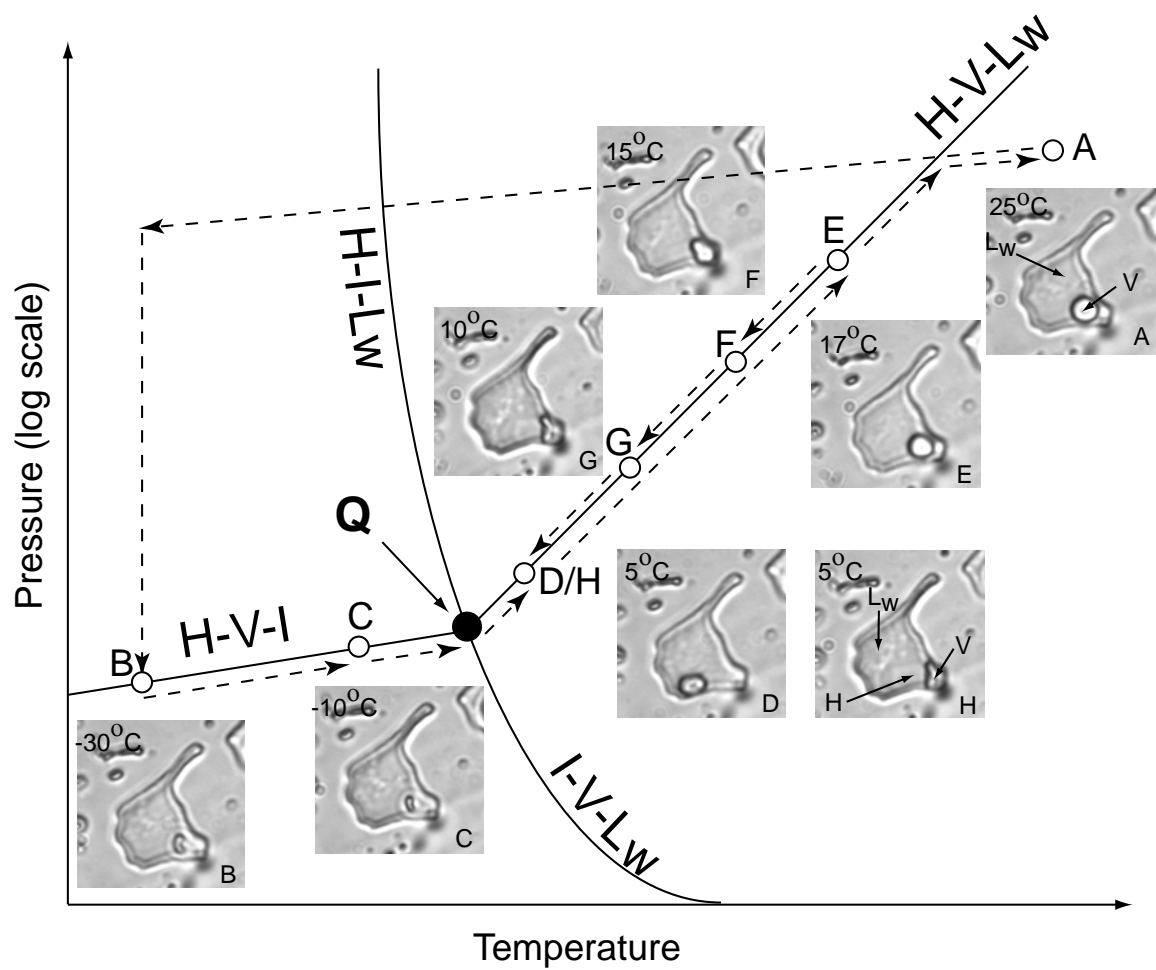


Figure 1. Phase behavior of a representative H₂O-CH₄ synthetic inclusion during the hydrate formation and dissociation.



Figure 2. Structure of the pressure cell used for Raman analysis. The metal block on the back is a standard three-way, two-stem, 15,000 psi combination valve. The components at the front, from left to right, are an O-ring, a circular 3.2 mm thick silica glass window, a brass gasket, a stainless steel retainer ring and a bullet-shaped bolt, respectively. The first four parts were put into the top hole of the valve in the order to seal the top window, the bullet-shaped bolt was inserted into the side hole on the right of the valve as a bleeding channel.

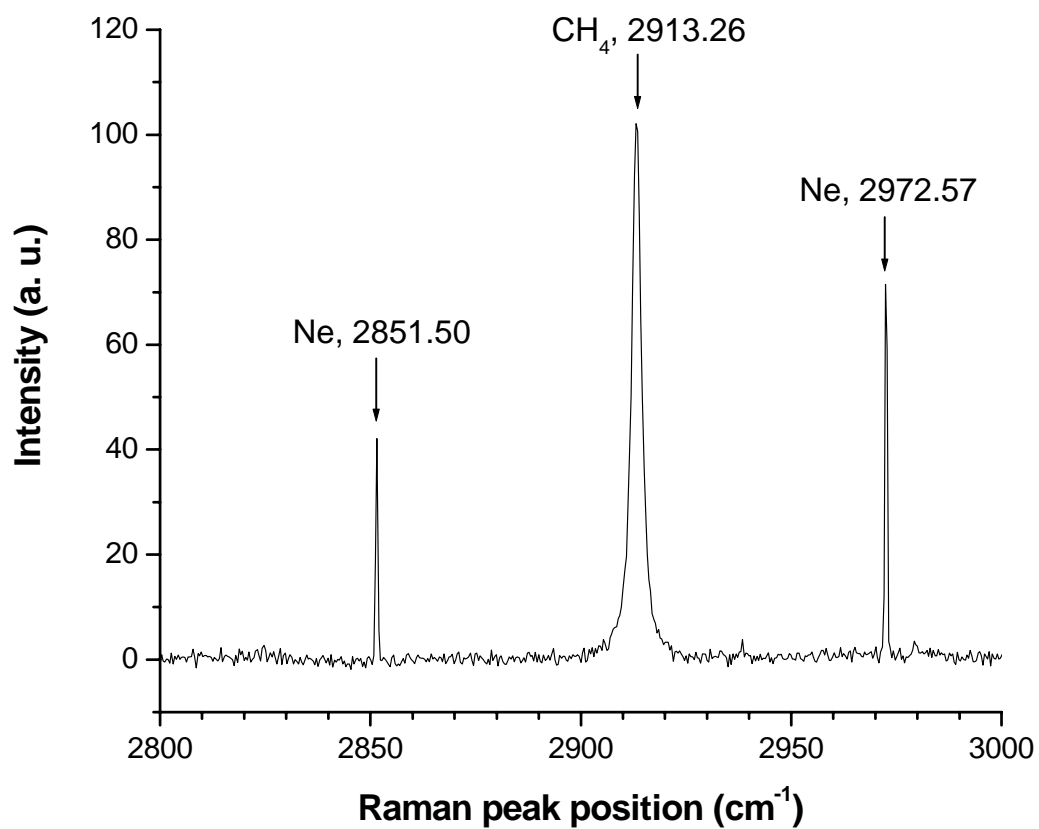


Figure 3. An example of simultaneously collected CH₄ and Neon Raman spectra. The CH₄ peak occurring at 2913.26cm⁻¹ is bracketed by the two emission lines of neon light appearing at 2851.50cm⁻¹ and 2972.57cm⁻¹.

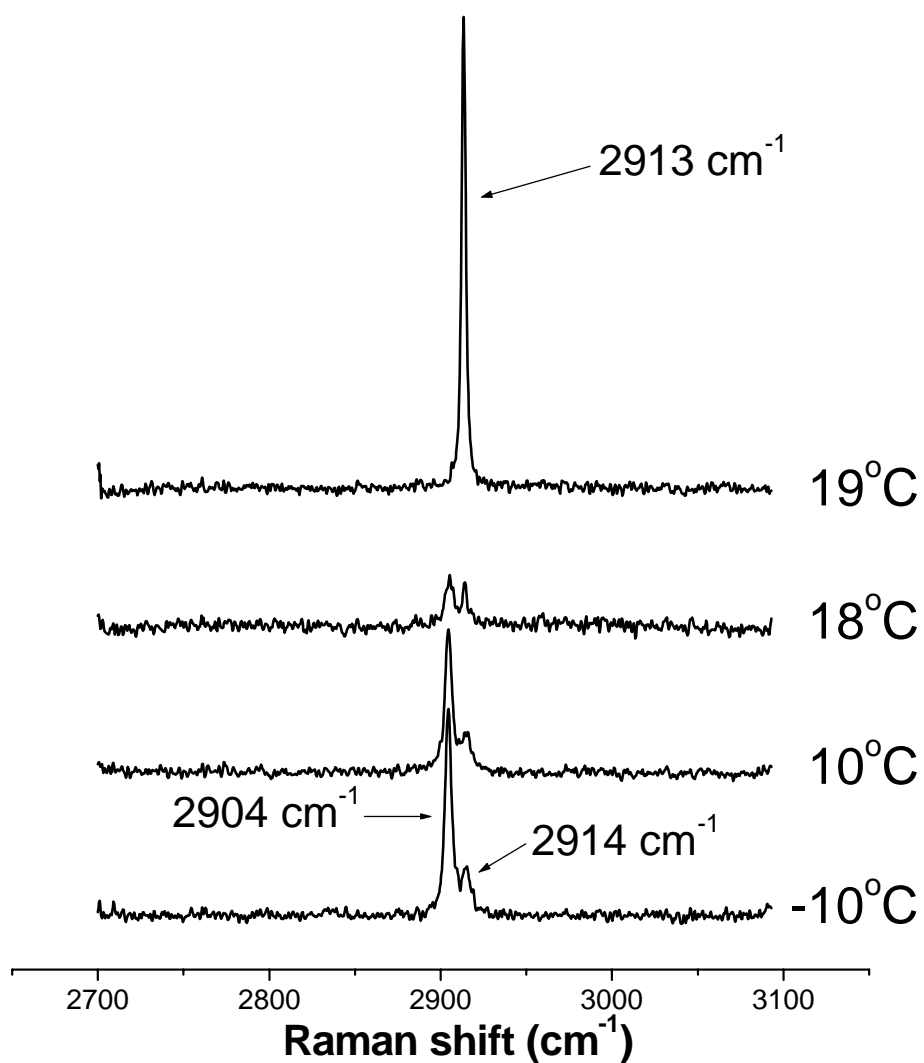


Figure 4. Raman spectra of methane hydrate at different temperatures. Note the spectrum changed from a doublet peak at 2904 and 2914 cm⁻¹ to a single peak at 2913 cm⁻¹ from 18°C to 19°C, representing the methane hydrate dissociated into a single methane gas phase.

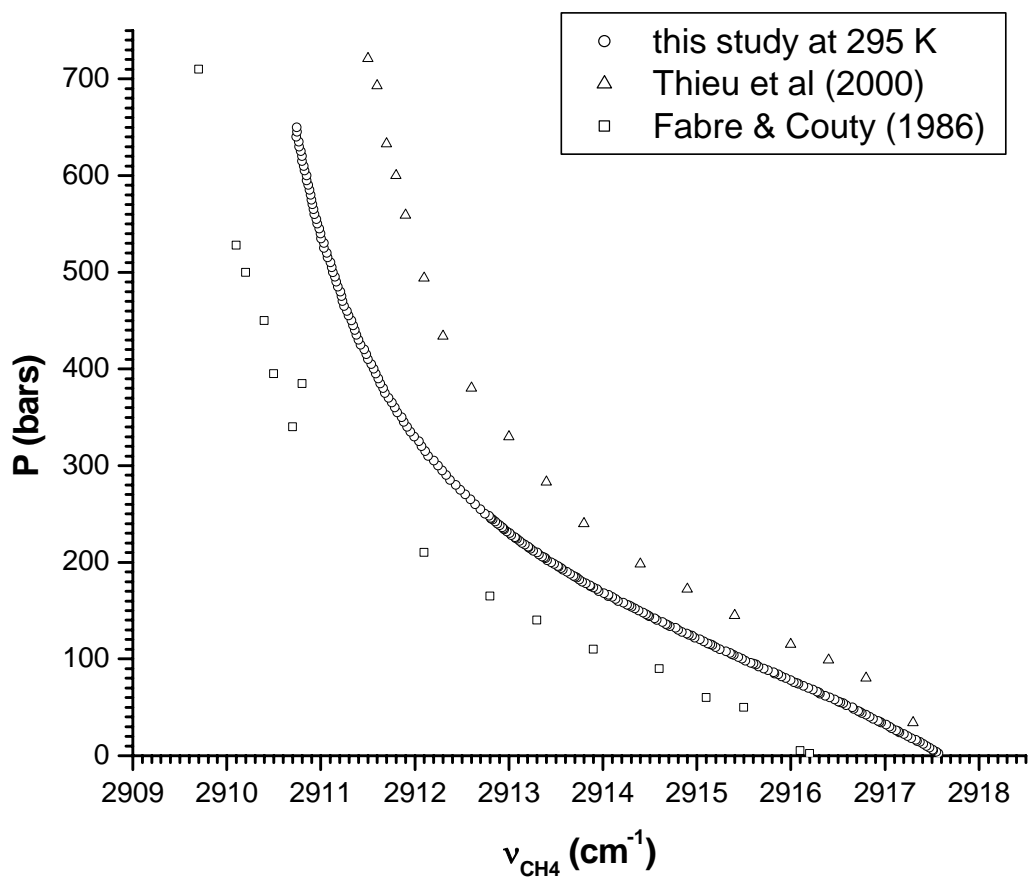


Figure 5. Comparison of the relationship between CH₄ Raman peak position and pressure reported in different studies.

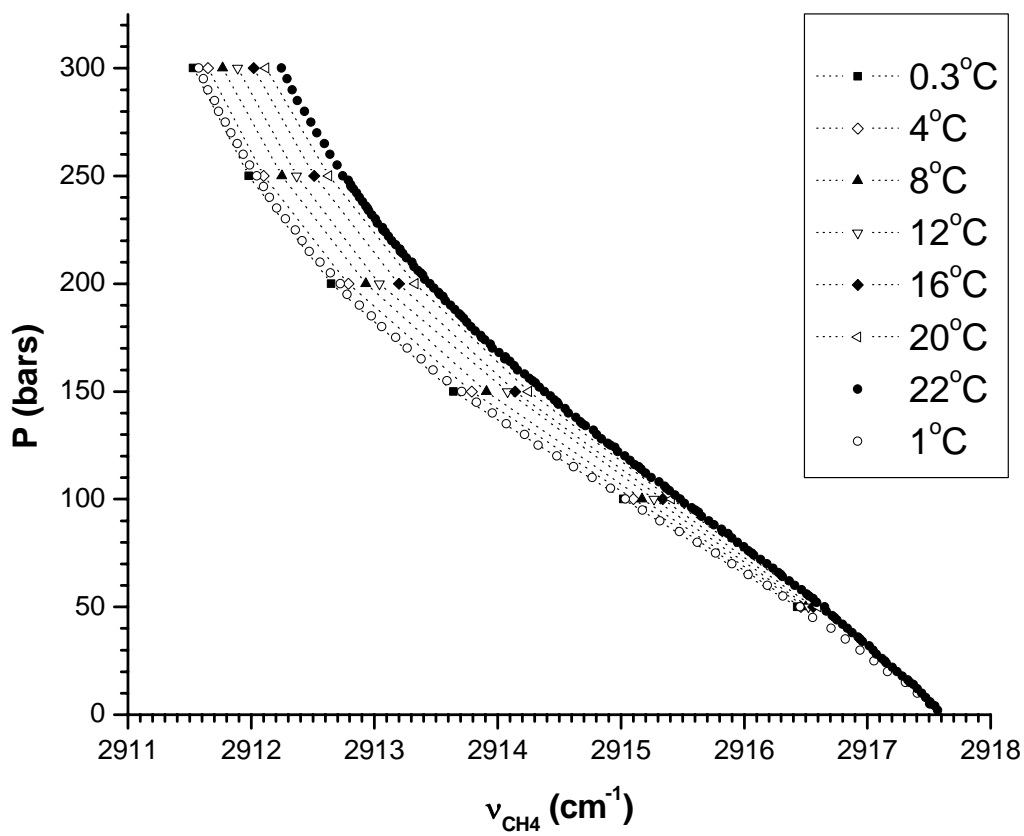


Figure 6. Pressure and temperature effect on methane Raman peak position between 0.3 to 22°C, 1 to 300 bars.

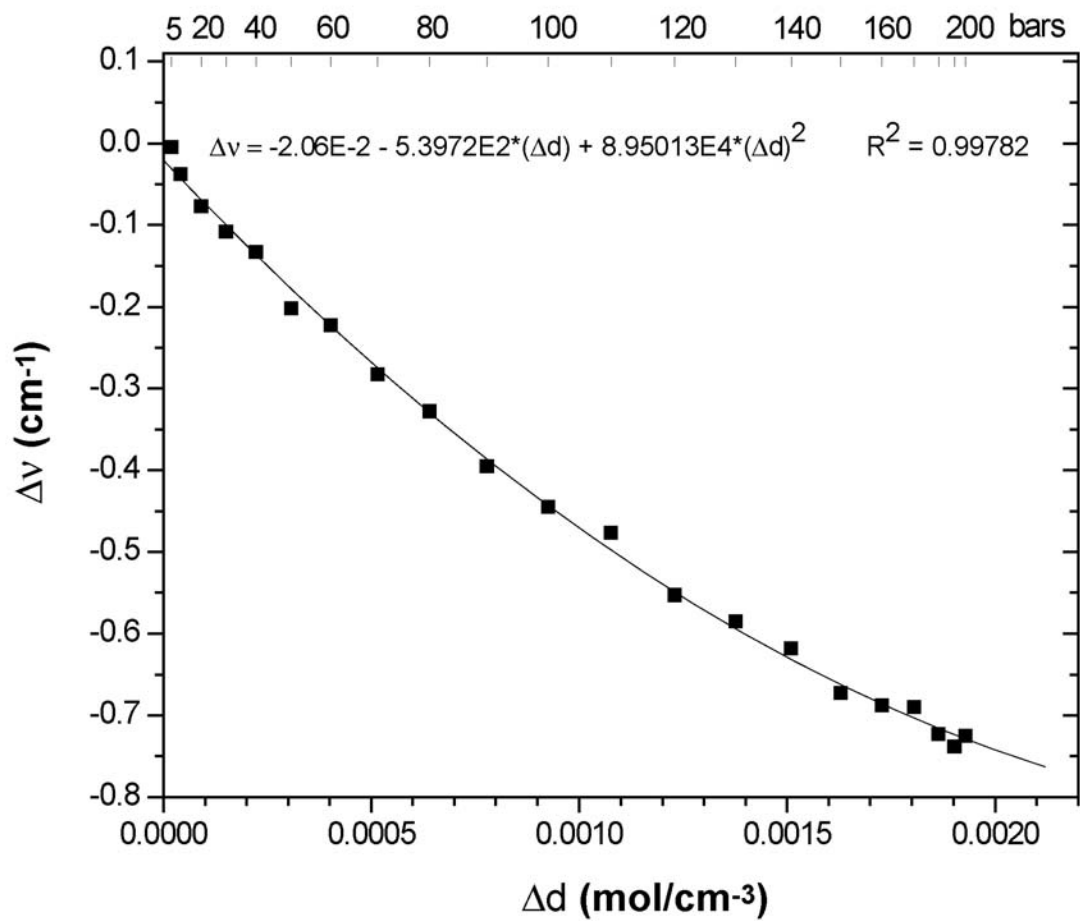


Figure 7. Change of CH₄ Raman peak position with the change of density of CH₄ as temperature drops from 295K to 270K in the pressure range of 5-200 bars.

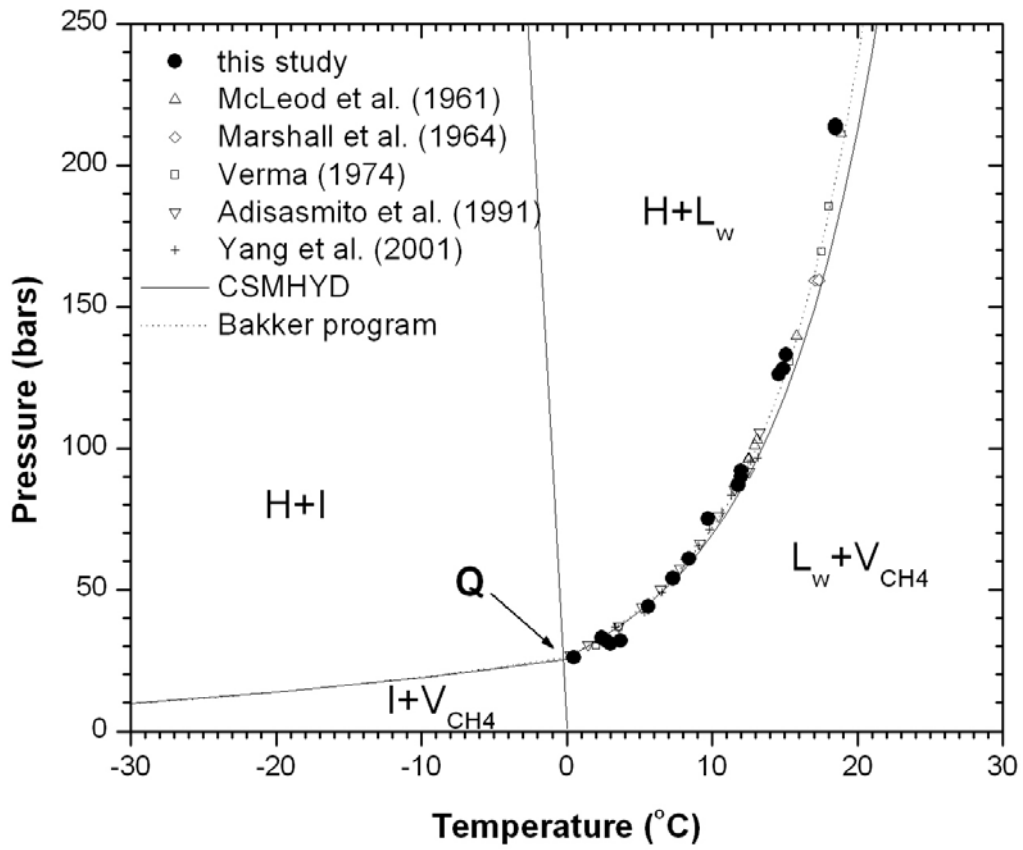


Figure 8. P-T stability limits of methane hydrate determined from the hydrate final melting conditions of 17 synthetic fluid inclusions, in comparison with data from theoretical models and some of experimental data from previous research.

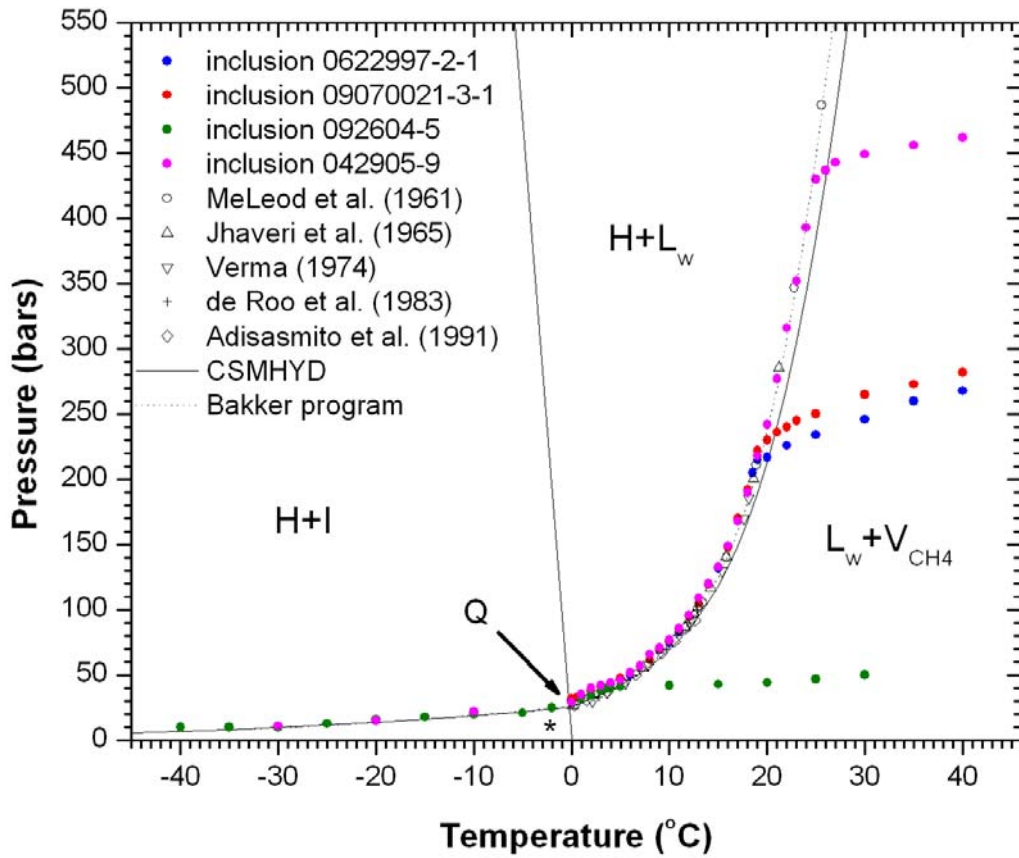


Figure 9. P-T stability limits of methane hydrate determined at the H-V-L_w and/or H-V-I equilibria of 4 synthetic fluid inclusions, in comparison with data from theoretical models and some of experimental data from previous research. The field labeled with an asterisk (*) is the I+V_{CH₄} field.

Chapter 4

Methane Raman ν_1 band position correlates with fluid density and interactions at the molecular level

Fang Lin¹, Amadeu K. Sum² and Robert J. Bodnar¹

1. Department of Geosciences, 2. Department of Chemical Engineering
Virginia Polytechnic Institute and State University, Blacksburg, VA 24061, USA

Abstract: The CH₄ Raman symmetric stretching ν_1 band position has been measured at various temperatures and pressures over the range 1-600 bars and 0.3-22°C. The C–H symmetric stretching band shifts to lower wavenumbers with increasing pressure and/or decreasing temperature, and shows a linear correlation with the change in density over this same range. *Ab initio* calculations show that the change in peak shape and position reflects the distortion of the methane structure as the density increases.

Methane (CH₄) has received attention from researchers in diverse fields because it is a major component of natural gas (1), represents a major contributor to global warming (2) and has been detected in the atmosphere or at the surface of extraterrestrial bodies (3-7). Interest in the properties of methane has also been stimulated by the discovery of large deposits of methane hydrate, a compound in which methane molecules reside in cages formed by water molecules (8), owing to the potential of methane hydrate as a future energy resource (9,10) and as a potential hazard to travel by sea (11).

Raman spectroscopy is a vibrational spectroscopic technique that monitors differences between the frequency of the incident laser and that of the stimulated Raman scattering from the investigated material. The Raman peak position, peak width and peak intensity reflect the microenvironment of the investigated molecules in terms of the atoms

involved in bonding, the bond length, bond strength, and polarizability (12-13). The two Raman active vibrational modes for CH₄ are the symmetric stretching mode and the twisting mode, usually denoted as ν_1 and ν_2 , respectively (14).

Previous research has shown that the ν_1 peak position is pressure-dependent and shifts systematically from $\sim 2917\text{ cm}^{-1}$ at 1 atm to lower wavenumber as pressure increases (15-18). Under extremely high pressures (0.6-18 GPa; 19), the trend is reversed for solid methane. In contrast, little is known about the effect of temperature on the ν_1 peak position. The few studies that have been conducted either focused on temperatures below the H₂O ice-melting temperature (20), or investigated CH₄ dissolved in aqueous solution at elevated temperature (21). A detailed understanding of the effect of pressure *and* temperature on CH₄ Raman line shift is not available.

A high-pressure optical cell mounted on the Raman microprobe was used to monitor the CH₄ Raman peak position as a function of temperature and pressure. The cell was made from a standard three-way, two-stem, 15,000 psi combination valve (High Pressure equipment, Model #10-15AF6) made from 316 stainless steel. A 1/2 inch, threaded hole was drilled into the center of the cell and halfway through the thickness. A smaller hole was then drilled from the bottom of this hole to a distance of 16 mm from the bottom of the valve body. An O-ring and circular 3.2 mm thick silica glass window were inserted into the hole and held in place with a stainless steel retainer ring. The cell is connected to a manual pressure generator (High Pressure equipment Model #50-6-15) that generates the desired pressure. The pressure in the cell was monitored using a Precise Instruments pressure transducer (Model 645), accurate to $\pm 0.1\%$ of the output pressure. Methane loaded into the pressure cell was of ultra-high purity grade. The system was

purged several times before each experiment to remove any other gases and/or water from the system.

For experiments at temperatures below ambient room temperature ($\approx 22^\circ\text{C}$), the pressure cell was immersed in a temperature-controlled water bath. The temperature was measured using an Omega type-E thermocouple, calibrated against the freezing point of water at 0°C , and was inserted into a small hole drilled into the top of the pressure cell, 10 mm deep and 5 mm from the gas chamber.

The Raman microprobe is a JY Horiba (800 mm) LabRam HR equipped with a 514.5 nm Laser Physics Ar⁺ laser. An Olympus BX41 microscope with a 3.5x objective was attached to the microprobe to accommodate the pressure cell and for observation and focusing the laser. The laser output was 50mW at the source. The spectrograph contains 1800 grooves/mm gratings which, combined with a slit width of 150 μm , resulted in a spectral resolution of $\pm 1.37 \text{ cm}^{-1}$ (22). The detector is an electronically-cooled CCD detector, operating normally at -70°C . At each P - T condition, five one-second spectra were collected.

Raman spectra were collected at 13 different temperatures (0.3, 1.0, 2.0, 4.0, 6.0, 8.0, 10.0, 12.0, 14.0, 16.0, 18.0, 20.0 and 22.0°C). Spectra were collected in 2 bar increments in the 1-250 bar range and in 5 bar increments in the 250-600 bar range at 22°C . For all other temperatures, the maximum pressure was 300 bars. Spectra were collected in 5 bar increments at 1°C and in 50 bar increments at all the other temperatures. Raman peak positions were recorded both during increasing pressure and decreasing pressure cycles. The mean value of the two measurements at each pressure was taken as

the Raman peak position at that pressure, although the difference between the two measurements was generally less than $\pm 0.03 \text{ cm}^{-1}$.

Due to the nonlinear behavior of the monochromator, the spectrometer position was calibrated in the spectral region of interest to optimize accuracy of the peak position measurement. A neon calibration lamp was installed in the optical path of the Raman microprobe, and two emission lines that bounded the methane peak were recorded simultaneously with the CH_4 Raman peak (see Fig. 1. The Ne lines used for calibration located at 2851.50 and 2972.57 cm^{-1} , bracket the CH_4 peak located at 2913.26 cm^{-1}). According to McCreery (23), the actual positions of the two Ne lines are 2851.38 and 2972.44 cm^{-1} , respectively, relative to a 514.5 nm laser. Using the measured peak positions for the CH_4 symmetric stretching band and the measured and real peak positions for the two Ne emission lines, the corrected (real) position for the methane peak (2913.14 cm^{-1} for the example in Fig. 1) is given by the following expression:

$$\nu_{corr}^{CH_4} = \frac{1}{2} \{ [\nu_{meas.}^{CH_4} + (\nu_{real}^{Ne,2851.38} - \nu_{meas.}^{Ne,2851.38})] + [\nu_{meas.}^{CH_4} + (\nu_{real}^{Ne,2972.44} - \nu_{meas.}^{Ne,2972.44})] \}$$

The position of each Raman line was determined using Gauss/Lorentz peak fitting after base line correction.

Recording the two Ne emission lines simultaneously with the CH_4 Raman peak during each collection is necessary for accurate location of the peak position. We have found that the Ne emission lines systematically shift to higher frequency with time and can shift up to 0.5 cm^{-1} over a few hours. Fortunately, the distance between the two Ne lines is constant at $121.06 \pm 0.03 \text{ cm}^{-1}$, allowing accurate determination of the CH_4 Raman peak position.

Along an isotherm, the peak position systematically shifts to lower wavenumber as pressure increases (Fig. 2). The shift is nearly linear at approximately 0.023 wavenumbers per bar up to 150 bars, and becomes less pressure dependent at higher pressures (Fig. 2). Under isobaric conditions, the peak position shifts to lower wavenumber as temperature decreases from 22 to 0.3°C. The temperature dependence of the Raman peak shift is small at pressures lower than about 50 bars, but becomes significant at higher pressures. For example, a peak position of 2912 cm⁻¹ corresponds to about 325 bars at 22°C, but at 1°C this same peak shift corresponds to about 255 bars.

The effect of temperature and pressure on the CH₄ Raman peak position correlates with the manner in which the CH₄ density varies over this same *P-T* range. Figure 3 shows the change in density (Δd) of CH₄ at various pressures between 5 to 200 bars when the temperature drops from 295K to 270K. The data of Raman peak position are from this study, the density data are Friend et al. (24). The good correlation between the CH₄ Raman peak shift and the density change of CH₄ suggests that the shift in Raman peak position represents a fundamental change in the nature of bonding in the methane molecule as density changes and interactions between molecules change. In order to explain the frequency shift and peak broadening of the ν_1 symmetric stretch for CH₄ (Fig. 2), *ab initio* calculations of the electronic structure were performed. These calculations provide insights into fundamental changes in the structure and vibrational modes for methane with changing density. We were particularly interested in determining the effect of pressure (or density) on the ν_1 symmetric stretch for methane. From a molecular point of view, higher density translates to methane molecules being closer to each other and to more frequent collisions.

Our approach was to use *ab initio* calculations to study the interaction of methane in clusters with two or three molecules. We have chosen clusters with only two or three molecules because those will be the most likely collisions to be encountered and the system size is computationally accessible. A single methane molecule was initially considered, however, it did not provide the desired results since the phenomena we want to capture is due to the collective interaction among molecules. All calculations were performed with the Gaussian03 suite of programs (25) using the MP2 (second order Moller-Plessett perturbation) method including all core electrons. The basis-set employed was the augmented Dunning's set with triple valence (aug-cc-pVTZ). All structures were optimized (tight convergence) at this level (MP2/aug-cc-pVTZ), as well as the resulting vibrational spectra at the optimized configuration.

All calculations were performed with the molecules in vacuum (i.e., there are no external influences on molecular structure). Thus, from these calculations, it is not possible to establish a direct relationship between the conditions used in the calculations and those found experimentally. However, we can qualitatively infer the relative changes that occur with increasing pressure. At low pressure (low density), it is reasonable to assume that molecules are far apart and are undisturbed by the presence of others (mean free path (λ) at 22°C and 1 bar is about 279 Å (26). As the pressure (density) increases, the mean free path decreases (at 10 bar, $\lambda = 28$ Å and 50 bar, $\lambda = 5.6$ Å – assuming an ideal gas). As the molecules come closer together, interactions between the molecules increase with greater probability for collisions (more frequent and stronger) such that one molecule affects the chemical environment of others. At high enough pressures, methane

becomes a supercritical fluid where the chemical environment is similar to a dense-fluid, and the molecules are close to one another.

In order to simulate the conditions described, we performed calculations that represented low- and high-pressure (or density) states. For low pressure, we considered two CH₄ molecules separated by 5 Å (carbon-carbon distance). As the pressure increases, the intermolecular distance between CH₄ molecules decreases, therefore, we considered the cases for two CH₄ molecules separated by 5.0, 4.0, 3.0, 2.6, 2.55 and 2.5 Å. In the supercritical state, multi-body effects become more prevalent, so we also considered three CH₄ molecules separated by 3.0, 2.8, 2.7, and 2.6 Å from each other (carbon-carbon distance). Figure 4 shows sample configurations for the two and three cluster cases.

For each of the configurations considered, the separation distance between CH₄ molecules was fixed and an optimization was performed to obtain the minimum energy state. The optimized configuration was then used to calculate the vibrational state of the molecules. For comparison, we also calculated the vibrational frequencies of a single isolated CH₄ molecule. Table 1 summarizes the results in terms of the geometry of the clusters and the frequency for the ν_1 symmetric stretch. Note that the frequencies reported have been scaled; the scaling factor was determined as outline by the NIST CCCBD (27).

As shown in Table 1, the structure and chemical environment of CH₄ significantly changes as molecules interact with one another. For two CH₄ molecules, we see a distortion of the molecules in terms of the C–H bond lengths. For the optimized configurations, three of the hydrogens for each molecule are pointing toward each other, while one hydrogen in each molecule is pointing away (see Fig. 4). As the separation distance between the molecules decreases, the bond length for the hydrogens facing each

other decreases, whereas the bond length for the hydrogen pointing in the opposite direction increases. This distortion of the methane geometry (compared to the isolated molecule) reflects the interaction of the molecules and the changes in structure due to their proximity to other molecules. The lengthening and shortening of the C–H bond lengths impact the vibrational modes. At low pressure, there is little interaction and collision between molecules, therefore essentially all molecules have C–H bond lengths near the equilibrium value, resulting in a narrow, sharp peak for the ν_1 vibrational frequency. As pressure increases, molecules begin to interact, leading to more frequent collisions. The collisions induce distortion of the C–H bonds, some contracting and some stretching from the equilibrium bond length. Not all bonds will be distorted to the same extent, thus, there will be a distribution of bond lengths, which leads to a range of values for the ν_1 vibrational frequency that is manifest as broadening of the measured band.

The symmetric stretching band also broadens because of the collective vibration of the molecules when in close proximity. As seen in Table 1, the ν_1 symmetric vibrational frequencies have two values at each separation distance. Both values correspond to the symmetric vibrational mode, however, one comes from the in-phase and the other from the out-of-phase interaction between molecules (Fig. 5). When molecules are in close proximity, the vibrational frequency is coupled to the intermolecular interactions. This relationship is more clearly seen when we consider the vibrational frequency of a single methane with its geometry set to that optimized with two molecules. For illustration, we chose the geometry for methane obtained at a separation distance of 2.5 Å. The ν_1 symmetric vibrational frequency for this single methane is 2914.36 cm^{-1} , which is about 4 cm^{-1} higher than those reported in Table 1 for

the two molecules, thus reflecting the effect of electron correlation between the two molecules.

The results shown in Table 1 for the two molecule cases show that at large separation distances ($> 5.0 \text{ \AA}$) the geometry of CH_4 is undisturbed, and consequently the ν_1 symmetric vibrational frequencies are the same as an isolated molecule. As the separation distance between two CH_4 molecules decreases, the distortion in the geometry leads to an increase in the ν_1 symmetric vibrational frequency to about 2.6 \AA . For distances less than about 2.55 \AA there is a shift in the trend, and closer proximity of the molecules results in a decrease in the ν_1 symmetric vibrational frequency. A similar behavior is observed when considering the cluster with three CH_4 molecules. A shift to lower frequency for the ν_1 symmetric vibrational mode is only seen at distances less than about 2.8 \AA . Distances greater than about 2.8 \AA show a shift to higher frequency, and as with the two methane cluster, we would expect the vibrational frequency to be unaffected for large distances (calculations were not performed for distances greater than 3.5 \AA).

The shift in the vibrational frequency as the separation distance changes is related to deformation of the electronic structure, and thus polarizability, when CH_4 molecules approach each other. At distances less than 2.55 and 2.8 \AA for the two and three molecules clusters, respectively, the distortion of the electronic cloud, accompanied by a distortion of the geometry (bond lengths), is “offset” by the intermolecular interactions. When considering a collection of CH_4 molecules, in particular as the density increases, the vibrational modes from one molecule are coupled to those of another. The shift in vibrational frequency can be attributed to the energy transfer between the molecules, having the end effect of “weakening” or “strengthening” the bonds, thus affecting the

vibrational spectrum. Consider the case of a single isolated methane molecule; if the geometry of methane is distorted by slightly decreasing all bond lengths by 0.002 Å, the ν_1 symmetric vibrational frequency shifts to 2935 cm^{-1} . On the other hand, increasing all bond lengths by 0.002 Å results in a frequency shift to 2904 cm^{-1} (see results in Table 1). Shortening the bond has the effect of strengthening the bond, as it takes more energy to stretch the bonds, resulting in higher vibrational frequency. The opposite case weakens the bonds as it requires less energy to stretch the bonds, thus lower vibrational frequency. If frequency shifts were only due to distortion of the geometry (bond lengths), one could easily predict the frequency shifts. For example, for the two-methane cluster separated by 2.5 Å, the average bond length in each C–H bond of CH_4 molecule is 1.0809 Å. An extrapolation of the vibrational frequency for this bond length would yield 2943.85 cm^{-1} , which is inconsistent with the actual calculated value of about 2910 cm^{-1} .

In qualitative terms, the *ab initio* calculations provide insight into molecular interactions that allow us to understand why the frequency of the ν_1 symmetric stretch for CH_4 shifts to lower wavenumbers as the pressure (or density) increases. One should keep in mind that the calculations performed here were for static configurations considering at most three CH_4 molecules. However, at laboratory conditions, the measurements involve dynamic systems in which molecules are colliding and bouncing in all directions. In order to obtain a more complete and quantitative confirmation of the observations, dynamic simulations (e.g., *ab initio* molecular dynamics) for a relatively large number of methane molecules (order of 10-20) would be required. This type of simulation is expected to yield the collective behavior of the system and ensemble averages that are more

representative of the actual experimental conditions, in terms of number of CH₄ molecules, temperature, and pressure/volume.

References

1. F. D. Mango, J. W. Hightower, A. T. James, *Nature* **368**, 536 (1994).
2. H. Rodhe, *Science, New Series* **248**, 1217 (1990).
3. D. P. Cruikshank, C. B. Pilcher, D. Morrison, *Science, New Series* **194**, 835 (1976).
4. G. L. Tyler *et al.*, *Science, New Series* **233**, 79 (1986).
5. H. B. Hammel, *Science, New Series* **244**, 1165 (1989).
6. H. B. Niemann *et al.*, *Science, New Series* **272**, 846 (1996).
7. J. S. Loveday *et al.*, *Nature* **410**, 661 (2001).
8. Sloan E. D., Jr. (1998) Clathrate hydrates of natural gases, 2nd. Ed. Marcel Dekker, New York.
9. K. A. Kvenvolden (1998) in Gas Hydrates, J.-P. Henreit, J. Mienert, Eds. (Geol. Soc. of London, Special Publication,) **137**, pp. 9-30.
10. K. A. Kvenvolden, *Ann. N.Y. Acad. Sci.* **912**, 17 (2000)
11. J. Marchant, *New Sci.* **2267**, 20 (December, 2000)
12. Long D. A. (1977) Raman Spectroscopy, McGraw-Hill, New York.
13. Long D. A. (2002) The Raman Effect: A Unified Treatment of the Theory of Raman Scattering by Molecules, John Wiley & Sons, Chichester.
14. T. Nishimura, F. Gianturco, *Phys. Rev. A* **65**, 062703-1, (2002).
15. A. D. May, J. C. Stryland, H. L. Welsh, *J. Chem. Phys.* **30**, 1099 (1959).
16. D. Fabre, R. Couty, *Comptes Rendu Acad. Sc. Paris* **303**, 1305 (in French) (1986).
17. J. C. Seitz, J. D. Pasteris, I. M. Chou, *Am. J. Sci.* **293**, 297 (1993).

18. V. Thieu, S. Subramanian, S. O. Colgate, E. D., Jr. Sloan, *Ann. N.Y. Acad. Sci.* **912**, 983 (2000).
19. Y. H. Wu, S. Sasaki, H. Shimizu, *J. Raman Spec.* **26**, 963 (1995).
20. M. A. Echargui, F. Marsault-Herail, *Molecular Physics* **60**, 605 (1987).
21. J. Pironon, J. O. W. Grimmer, S. Teinturier, D. Guillaume, J. Dubessy, *J. Geochem. Exploration* **78-79**, 111 (2003).
22. R. M. Paroli, I. S. Butler, *Appl. Spectro.* **44**, 1414 (1990).
23. McCreery R. L. (2000) Raman spectroscopy for chemical analysis. John Wiley & Sons, New York. 420pp.
24. Friend D. G., Ely J. F. and Ingham H. (1989) Tables for the thermophysical properties of Methane. NIST Technical Note 1325, U.S. Department of Commerce/National Institute of Standards and Technology.
25. Gaussian 03, Revision B.05, M. J. Frisch, G. W. Trucks, H. B. Schlegel, G. E. Scuse-ria, M. A. Robb, J. R. Cheeseman, J. A. Montgomery, Jr., T. Vreven, K. N. Kudin, J. C. Burant, J. M. Millam, S. S. Iyengar, J. Tomasi, V. Barone, B. Mennucci, M. Cossi, G. Scalmani, N. Rega, G. A. Petersson, H. Nakatsuji, M. Hada, M. Ehara, K. Toyota, R. Fukuda, J. Hasegawa, M. Ishida, T. Nakajima, Y. Honda, O. Kitao, H. Nakai, M. Klene, X. Li, J. E. Knox, H. P. Hratchian, J. B. Cross, V. Bakken, C. Adamo, J. Jaramillo, R. Gomperts, R. E. Stratmann, O. Yazyev, A. J. Austin, R. Cammi, C. Pomelli, J. W. Ochterski, P. Y. Ayala, K. Morokuma, G. A. Voth, P. Salvador, J. J. Dannenberg, V. G. Zakrzewski, S. Dapprich, A. D. Daniels, M. C. Strain, O. Farkas, D. K. Malick, A. D. Rabuck, K. Raghavachari, J. B. Foresman, J. V. Ortiz, Q. Cui, A. G. Baboul, S. Clifford, J. Cioslowski, B. B. Stefanov, G. Liu, A. Liashenko, P. Piskorz, I. Komaromi, R. L. Martin, D. J. Fox, T. Keith, M. A. Al-Laham, C. Y. Peng, A. Nanayakkara, M. Challacombe, P. M. W. Gill, B. Johnson, W. Chen, M. W. Wong, C. Gonzalez, and J. A. Pople, Gaussian, Inc., Wallingford CT, 2004.
26. McQuarrie D. A. (1973) Statistical Mechanics. HarperCollins, New York.
27. NIST Computational Chemistry Comparison and Benchmark Database, NIST Standard Reference Database Number 101, Release 12, Aug 2005, Editor: Russell D. Johnson III, <http://srdata.nist.gov/cccbdb>
28. Herzberg G. (1966) Electronic spectra and electronic structure of polyatomic mole- cules. Van Nostrand, New York.
29. Shimanouchi T. (1972) Tables of Molecular Vibrational Frequencies, Consolidated Volume 1, NSRDS NBS-39.

Table 1. Summary of results obtained from *ab initio* calculations (MP2/aug-cc-pVTZ) for methane. Light and dark shaded areas correspond to the configuration with two and three methane molecules, respectively.

Separation distance (Å)	C-H bond length (Å)	Frequency ν_1 (cm ⁻¹) [‡]
Experimental	1.0940 ^a	2917 ^b
single [*]	1.0841	2918.88
single ^{**}	1.0820	2935.37
single ^{**}	1.0860	2904.18
2.50	1.0772 ^c / 1.0920 ^d	2909.63 / 2910.59
2.55	1.0780 ^c / 1.0908 ^d	2916.66 / 2917.18
2.60	1.0788 ^c / 1.0898 ^d	2921.60 / 2921.60
3.00	1.0826 ^c / 1.0857 ^d	2924.87 / 2925.94
4.00	1.0841 ^c / 1.0845 ^d	2919.31 / 2919.73
5.00	1.0841 ^c / 1.0842 ^d	2918.56 / 2919.10
2.60	1.0660 ^e / 1.0831 / 1.0962	2882.03 / 2883.43
2.70	1.0695 ^e / 1.0832 / 1.0932	2904.77 / 2905.19
2.80	1.0726 ^e / 1.0834 / 1.0909	2918.75 / 2918.75
3.00	1.0775 ^e / 1.0839 / 1.0878	2928.80 / 2928.85

[‡] calculated frequencies scaled by a factor of 0.9473

^{*} single methane molecule fully optimized (no constraints)

^{**} single methane molecule; all bond lengths constrained to given value

^a from Herzberg (28)

^b from Shimanouchi (29)

^c bond length for three of the bonds in each methane molecule

^d bond length for one of the bonds in each methane molecule

^e bond length for two of the bonds in each methane molecule

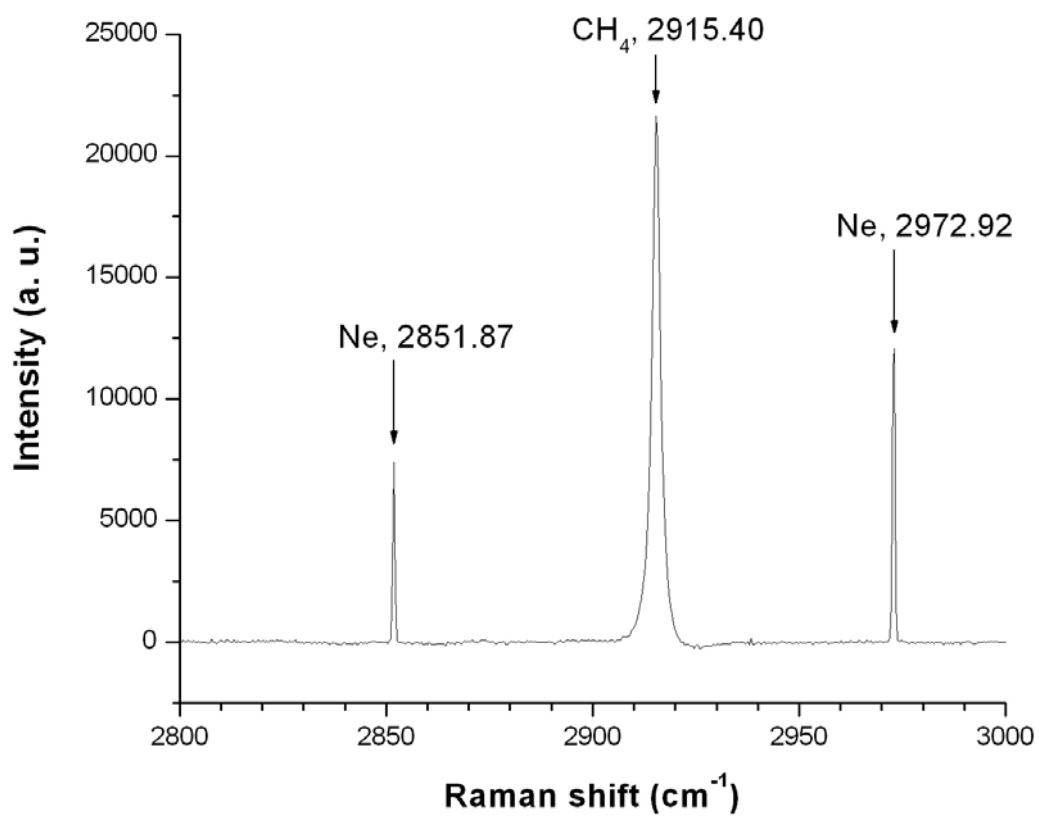


Figure 1. CH₄ peak collected together with Neon peaks. The CH₄ peak occurring at 2913.26cm⁻¹ is bracketed by the two Ne Raman peaks at 2851.50cm⁻¹ and 2972.57cm⁻¹.

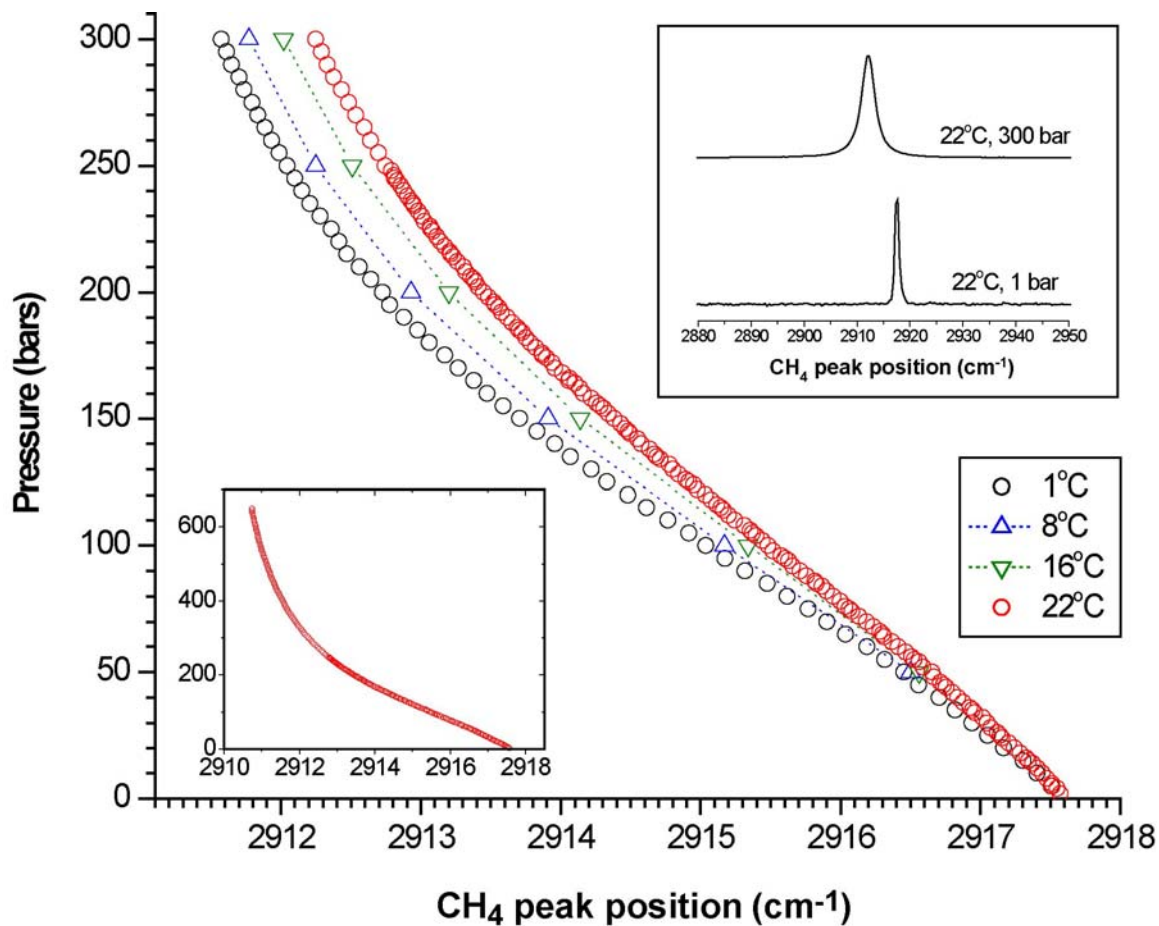


Figure 2. Pressure and temperature dependence of the Raman CH₄ C-H symmetric stretching band at 1°, 8°, 16° and 22°C. The inset in the upper right shows the Raman spectrum of CH₄ at 22°C and 1 (bottom) and 300 (top) bars. The inset in the lower left shows the peak shift at 22°C up to 600 bars.

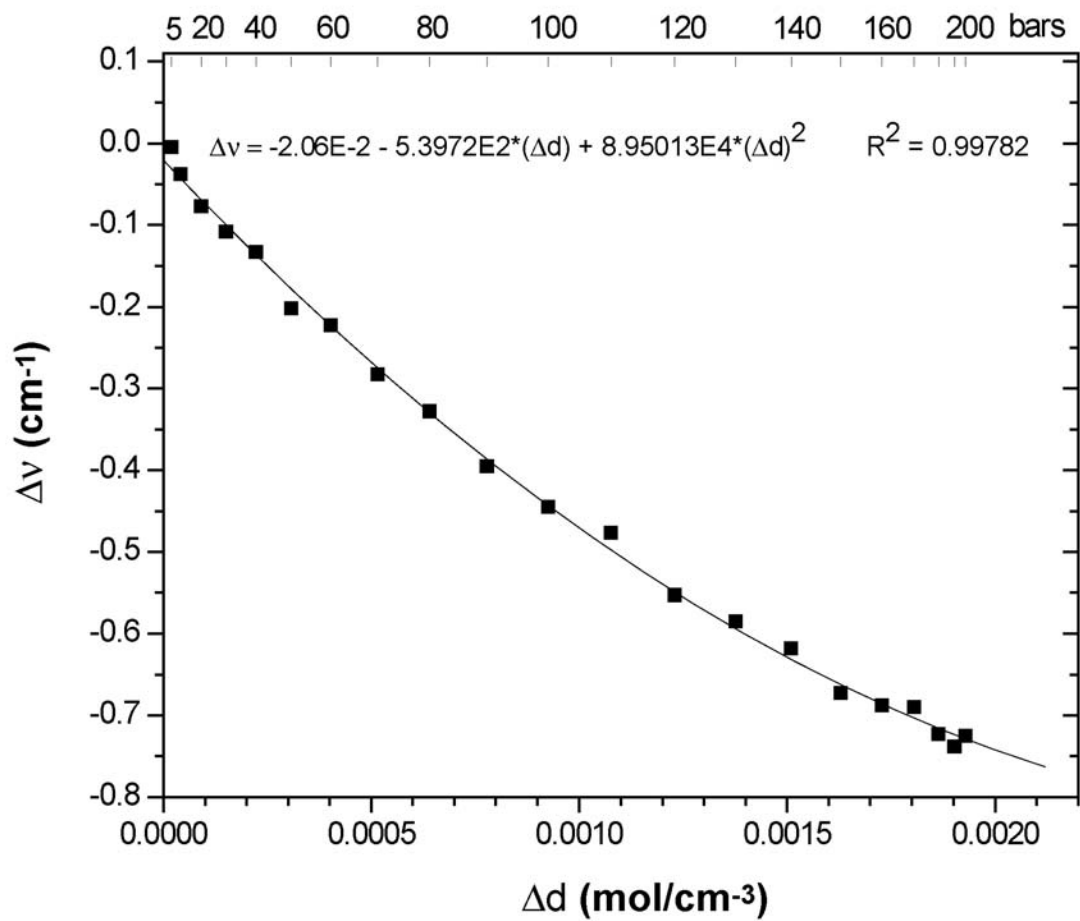


Figure 3. Change of CH₄ Raman peak position with the change of density of CH₄ as temperature drops from 295K to 270K in the pressure range of 5-200 bars.

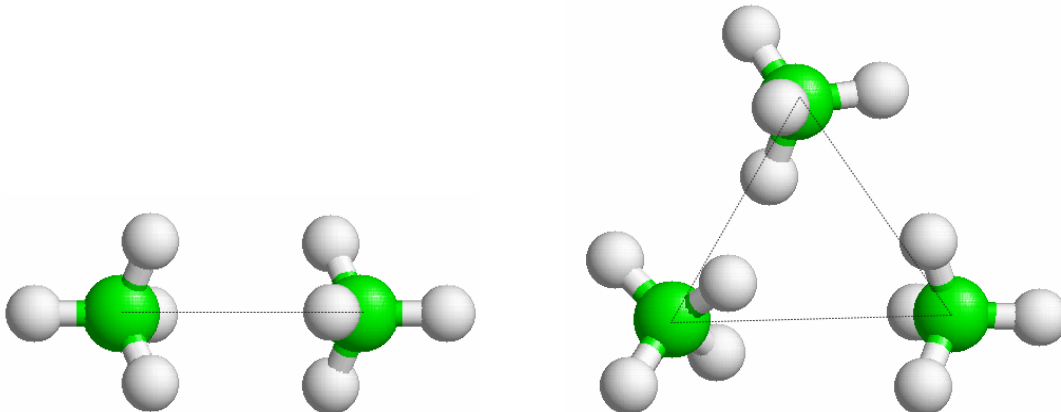


Figure 4. Sample configuration for the two (left) and three (right) CH₄ molecules considered in the calculations. In the energy minimization of the structures, the distance between the molecules was fixed at 3.0 and 3.5 Å for the two and three molecules, respectively, shown in the figure. Final structures were used in the calculation of the vibrational spectra. All calculations were performed using MP2/aug-cc-pVTZ.

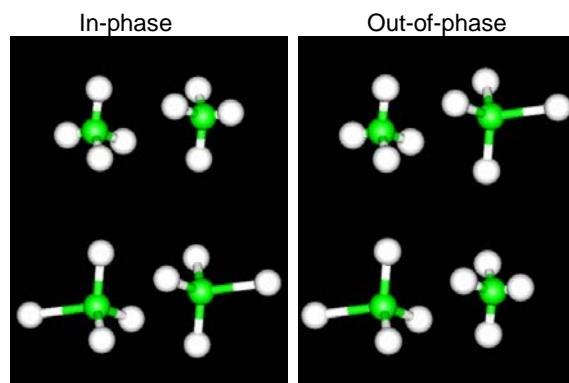


Figure 5. Sample configurations illustrating the two modes of vibration for the ν_1 symmetric vibrational stretch between two CH₄ molecules. In the in-phase mode, both molecules either stretch or contract their bonds at the same time, whereas in the out-of-phase case, while the bonds for one molecule are stretched, the ones for the other are contracted. The resulting vibrational frequency for the two modes differs by about 1 cm^{-1} .